Quantitative Imaging and Tomography with Polychromatic X-rays

Yiyue Huang

A thesis submitted for the degree of
Bachelor of Philosophy with Honours in Physics at
The Australian National University

October 2023

Declaration

This thesis is an account of research undertaken between [February 2023] and [October 2023] at the Research School of Physics, The Australian National University, Canberra, Australia.

Except where acknowledged in the customary manner, the material presented in this thesis is, to the best of my knowledge, original and has not been submitted in whole or part for a degree at any other university.

Yiyue Huang

October 2023

Acknowledgements

This thesis was supervised by A/Prof Andrew Kingston and Prof Adrian Sheppard of the Department of Materials Physics (DMP) at the Research School of Physics of the Australian National University.

I must first thank my supervisors Andrew and Adrian for their guidance and support throughout this project. This thesis could not have been completed without your guidance, optimism, and patience. Thank you both for your eternal patience and willingness to spend days and hours helping me sort the problems I have encountered and helping me obtain a deeper understanding of this project. It has been a really enjoyable journey to work with both of you, and I have learned more than I would expect during just one year. I would be really happy for any opportunity in the future to work together again.

I would also like to thank Benjamin Young for teaching and helping me with the X-ray system setups in experiments, also for making the testing step wedges and collecting extra data for testing. Thanks to Klara Steklova for modeling the X-ray source to help us understand the potential uncertainties in our experiments. I would thank everyone in the X-ray tomography and applications group that helped me understand the project from various perspectives.

Finally, I would like to thank my family and friends for supporting me throughout my studies.

Abstract

X-ray computed tomography (XCT) is a powerful tool, renowned for its ability to non-destructively produce highly-detailed 3D images of an object's internal structure. The scanning process captures X-ray projections of the object of interest from various angles and then computationally creates a volumetric map of its X-ray attenuation coefficient. Conventional lab-based XCT invariably employs polychromatic (or broadband) X-ray radiation. This causes imaging artifacts since attenuation (the reconstructed quantity) is a function of X-ray energy, making it difficult to differentiate materials, let alone obtain quantitative information. While some methods have been proposed in the literature, no effective approach has been widely applied.

In this work, we propose a two-material (2M) model for polychromatic multi-energy XCT. This model is an alternative to the well-known Alvarez-Macovski (AM) model, that approximates that X-ray attenuation for a material by a simple function of its density, atomic number, and the energy of X-rays. The 2M model assumes that X-ray attenuation for a material can be modeled by a linear combination of that of two known materials (basis materials). We can then effectively reconstruct a quantitative estimate of the material properties: density and atomic number, from those of the two basis materials. Moreover, since these models capture the energy-dependence of attenuation, they inherently account for common tomography artifacts.

In simulation tomography, the 2M model showed improved artifact correction and yielded quantitative results comparable to the AM model, with densities and atomic numbers having a relative error within 10%. Through experiments, we demonstrated that the 2M model can simplify laboratory XCT calibration. Unlike the AM model, which requires full spectrum knowledge, the 2M approach only needs measurements of X-ray attenuation for specific basis material combinations to approximate where our target material fits. While the 2M model exhibited some potential, we further identified its limitations in the lab and suggested future improvements for its mature implementation.

Contents

Chapter 1

Introduction

1.1 X-ray Computed Tomography (XCT): Working Principles and Applications

X-ray computed tomography (XCT) is a powerful tool that has become indispensable in volumetric imaging due to its capacity to generate intricate 3D scans of an object's internal structure without causing any damage [1]. Given that X-rays generally interact weakly with matter and have minimal refraction, i.e., they follow straight lines, they serve as a penetrating probe, making XCT versatile for various object sizes and compositions.

The XCT scanning process involves taking a series of X-ray images (also known as radiographs or projections) of the object of interest from various angles. The images collected are then processed using mathematical algorithms to reconstruct a 3D map of the object's internal structure. This map reveals the object property of X-ray attenuation, which is related to both density and atomic number (factors that form the basis for image contrast) of the materials inside the object. As the X-ray beam passes through the object, different materials attenuate (or absorb and scatter) the X-ray photons to varying extents. For instance, denser materials tend to attenuate more X-rays than lighter ones. This 3D representation is typically rendered in grayscale, wherein different materials correspond to distinct grayscale values, which can allow us to discriminate between certain materials within the object. Figure 1.1 shows an XCT image of a cross-section of a human head, with different grayscale values corresponding to various features such as the brain, skull, etc.

One of the standout qualities of XCT is its ability to probe non-destructively. Contrary to many other investigative methods that often involve invasive measures or modification

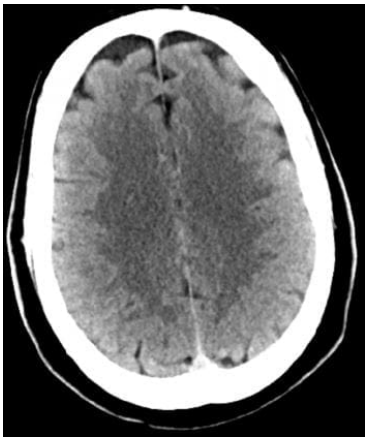

Figure 1.1: An XCT image of a cross-section of a human head, with varying grayscale values represent structures and features such as the brain, skull, and other anatomical details [2].

to the subject under study, XCT can reveal detailed insights into the internal composition of objects without any detrimental effects. Therefore, XCT can be used on living tissue as long as dose is taken into consideration. Moreover, the resolution of XCT can extend from nanometers to centimeters, even to meters. This unique capability makes it a preferred choice in a myriad of applications. One common implementation in our daily life is luggage scanning at airports [3]. In medical imaging, XCT is used for visualising structure of internal organs and bones, thereby facilitating the early detection of health concerns like tumors and infections [4]. XCT is also commonly used in industrial inspection for evaluation and quality control of manufactured products, such as electronics [5]. Furthermore, its applications extend to diverse sectors including material science [6], where it aids in analysing material properties, geoscience [7], where it contributes to understanding geological formations and phenomena, and archaeology [8], where it assists in the non-invasive study of historical artifacts and relics.

1.2 Motivation: Quantitative XCT and Its Practical Applications

While XCT is an excellent tool for understanding the internal structure of an object, it has limitations in detecting the actual composition, i.e., the material or chemical makeup of the object. The detailed reasoning behind this limitation is provided in Section 1.3. If

XCT could differentiate between the actual compositions within an object—quantifying physical properties such as density and atomic number—it could provide value to a great many more applications.

One example is that quantitative XCT could be used to detect the magnesium (Mg) content in the skeletons of certain marine organisms (e.g., corals, foraminifera, coralline algae). This is of interest to climate scientists because the Mg content can be related to climate indicators such as ocean temperature and salinity [9]. Quantitative XCT can also provide valuable insights into the effects of osteoporosis and bone remineralisation processes. Bone is primarily composed of collagen, hydroxyapatite (HA), and water in varying ratios, and it is generally assumed that the concentration of HA that determines bone rigidity and strength [10]. Quantitative XCT could effectively evaluate the amount of hydroxyapatite (HA) in bones. A third example is in mineral exploration, diamonds are exceptionally rare, and the presence of large diamonds is typically associated with many microdiamonds (diameter $< 100\,\mu m$). Imaging drill cores with XCT for microdiamonds is an ideal method to estimate the likelihood of finding larger diamonds. However, diamonds are hard to identify because they resemble sandstone at low X-ray energies and denser minerals at higher energies. Quantitative XCT could solve this problem and is a current research project in the Material Physics Department in ANU.

Unlike in medical imaging, where the elements inside the human body are known, in laboratory XCT, we typically do not have any information before scanning and reconstructing the image of the object of interest. Quantitative XCT generally provides geologists with the necessary information, such as material density and atomic number. It also allows for differentiation among materials that exhibit identical attenuation (grayscale values) in conventional reconstructed X-ray tomograms. Additionally, it can reduce X-ray beam-hardening artifacts that may distort automated analysis, a topic I will explore in the next section.

1.3 Artifacts in XCT Limiting Quantitative Analysis

As with any imaging technique, XCT is not immune to the presence of artifacts — various types of errors, inconsistencies, or distortions in the reconstructed tomograms that do not

correspond to the object's true structure or composition. Here, I explore the two main causes of artifacts: X-ray beam-hardening and X-ray scatter.

1.3.1 Beam-Hardening Artifacts

One of the most notable artifacts in XCT is X-ray beam-hardening [11]. Conventional laboratory XCT invariably employs polychromatic (or broadband) X-ray radiation and uses various filters to manipulate the incident energy spectrum of the X-ray beam [12]. Beam-hardening refers to the phenomenon wherein the lower-energy (or soft) X-rays are attenuated more readily or with a higher probability as they pass through any material. As a result, the remaining X-ray beam that emerges from the object and reaches the detector is 'harder' or has a higher average energy than the original beam [11]. Figure 1.2 shows the spectra after passing through a certain amount of Aluminum; the average energy of the spectrum shifts to a higher energy as it traverses more material.

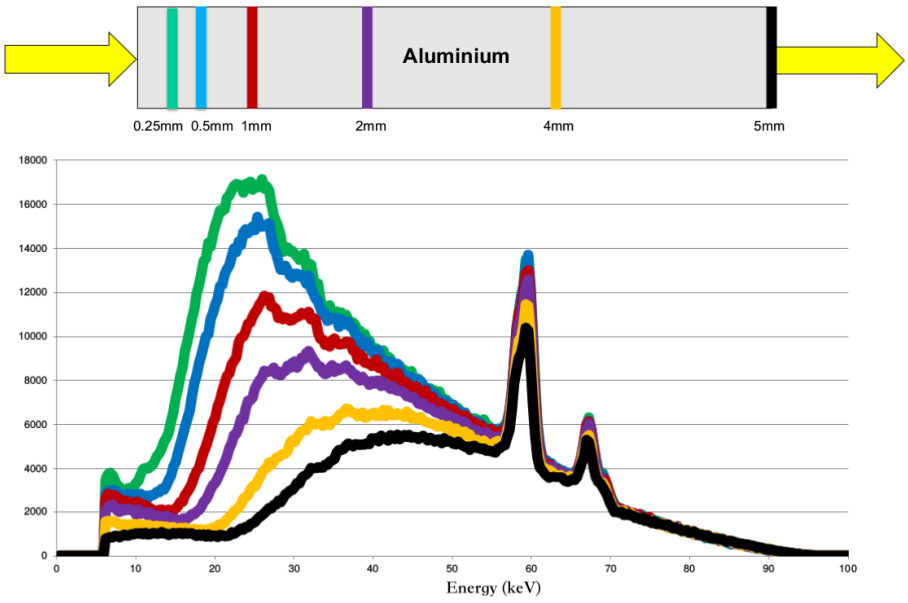

Figure 1.2: Spectrum after passing through different thickness of Aluminum (Image sourced from Mahsa Paziresh's presentation slides in [13]).

Beam-hardening can severely impact the accuracy of quantitative measurements made using XCT. For a specific incident X-ray spectrum, two or more materials inside an object might exhibit extremely similar grayscale levels in the reconstructed image. Unless each has a unique location or morphology, differentiating one from another becomes

challenging, let alone obtaining quantitative information. Beam-hardening affects XCT primarily by producing the following artifacts (see Figure 1.3): *cupping artifacts*, where the center of an object exhibits a lower attenuation coefficient than its periphery (the image profile exhibits a cup shape); and *streak artifacts*, which introduce unexpected lines or patterns into the reconstructed images [11].

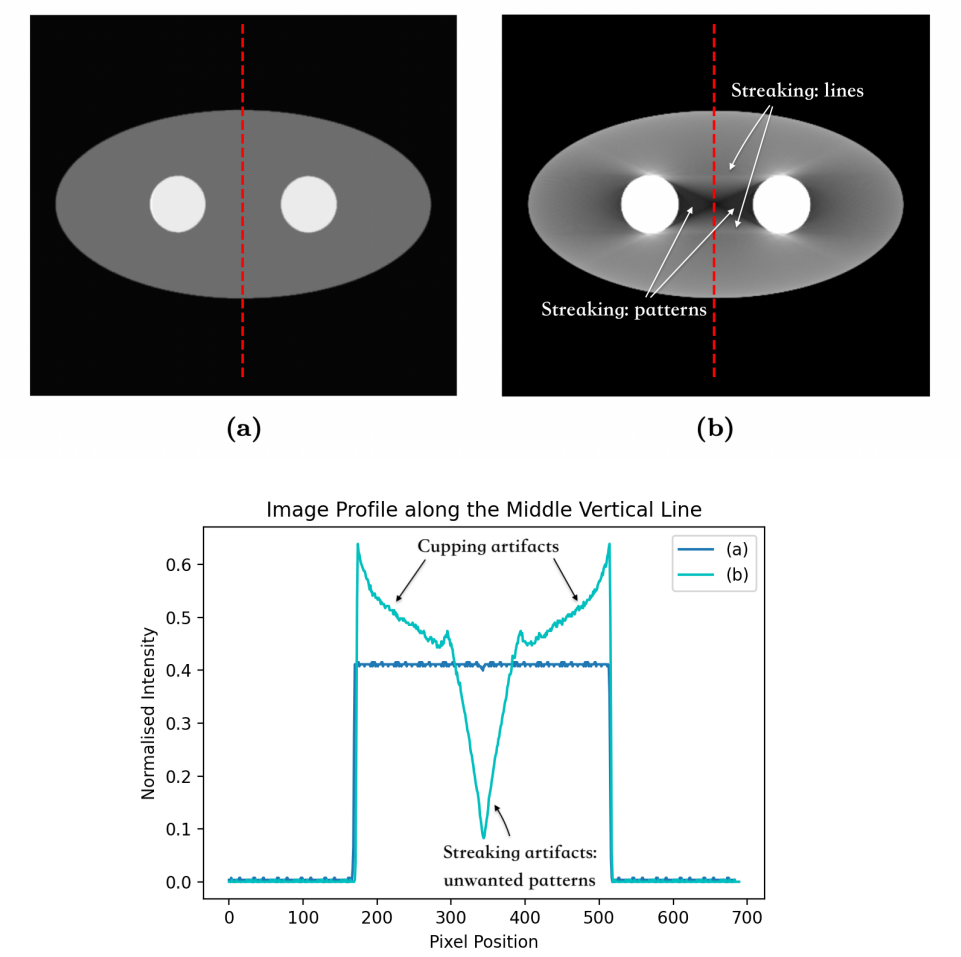

Figure 1.3: Beam-hardening example: a simulated sample consists of water (gray), bone (white) and air (black). (a) 2D slice through an 'ideal' volume reconstructed using a monochromatic X-ray beam (b) 2D slice through a volume reconstructed using a realistic polychromatic X-ray beam, with beam-hardening artifacts exhibited: cupping (edges brighter than the center) and streaking (unwanted lines and patterns) [14]. The image profile for both reconstructions along the middle vertical line (marked as red dashed lines) is shown below. The y-axis shows the normalised intensity (essentially the normalised grayscale values along the line), which illustrates cupping artifacts (values increasing towards the edge) and streaking artifacts.

1.3.2 Secondary Radiation Artifacts

Secondary radiation, often referred to as scattered radiation, is another artifact that degrades image quality in XCT. This scatter can originate from multiple sources:

1. **Scatter from the X-ray source (off-focal X-rays):** X-rays scattered inside the source tube as well as X-rays produced from electrons scattered inside the tube can produce off-focal radiation that diverges from the primary beam direction [15].

2. **Scatter from the object:** When primary X-rays penetrate and interact with an object, a portion of these X-rays is attenuated by Compton scattering, which causes them to be deflected from their original path and scatter in various directions [16]. A portion of these scattered X-rays will be detected by the detector.

3. **Scatter from the cabinet:** The imaging cabinet, designed to shield the surroundings from radiation, can contribute to scatter if residual X-rays reflect off its walls and are directed back towards the detector.

These scattered X-rays carry altered properties, i.e., they have a different spectrum and are not travelling from the primary focal point. As mentioned above, these X-rays can still reach the detector, thus introducing confounding data to the radiographic image being analysed.

The artifacts produced by scattered radiation manifests as a reduction in image contrast, the appearance of 'haze' or 'fog', and sometimes even streaks across the image [17]. Such artifacts can obscure fine details and lead to misinterpretations, particularly in situations where quantification or differentiation between materials is important.

Several strategies have been developed to reduce scatter artifacts, including hardware solutions like anti-scatter grids and software-based post-processing corrections [18]. Nevertheless, the complete elimination of scatter artifacts remains a challenge, especially in higher-energy imaging of large or dense objects where scatter is pronounced.

1.4 More about Quantitative X-ray Imaging: Beyond Beam-Hardening

In this project, among XCT artifacts, the one I focus on the most is dealing with beam-hardening artifacts in image reconstruction, and quantitative tomography reconstruction must inherently account for beam-hardening. This section provides an overview of existing approaches to mitigate beam-hardening artifacts. More details including their limitations will be presented in Chapter 3.

Numerous strategies that deal with beam-hardening artifacts have been developed to improve the quality of the reconstructed images. The simplest hardware approach in the lab is *beam filtration*. It uses filters made of uniform material to reduce the soft X-rays in the illumination beam, thereby reducing its potential to 'harden' as it traverses the object [19]. In situations where the sample attenuation is relatively low, this is an effective mitigation. The most common software approach is *linearisation*, which converts the measured X-ray attenuation values into equivalent 'ideal' values that a monoenergetic X-ray beam would produce when passing through different thickness of a particular material [20]. The most quantitative method is *multi-energy (or dual-energy) imaging* [21]. By acquiring images at two distinct X-ray energy levels, this method allows for differentiation of materials and correction of beam-hardening artifacts. The two sets of images are combined, drawing from the complementary information in each, to produce an image with reduced artifacts. More details of this approach will be presented in Chapter 3. Another potential method is *hyperspectral imaging* [22]. It substitutes the conventional detector with one that measures the photon energy of each X ray that arrives and constructs a spectrum for each pixel, making it possible to discriminate between materials with similar grayscale levels by comparing their differences in absorbed X-ray spectrum.

1.5 Project Goals and Thesis Outline

In medical imaging, the chemical elements inside the human body are known *a-priori*, known attenuation models can be employed for calibration and tuning of the incident

spectrum to produce contrast between important tissue types [20]. However, in laboratory XCT, where we do not have prior knowledge about the composition of an object, other techniques must be developed to properly identify the materials present.

Although the existing theoretical model has previously been proven valid through simulations, it has not been validated experimentally due to numerous complicating factors including secondary radiation artifacts. Given that some promising approaches have been developed to mitigate these issues in recent years [15], it is hoped that the theoretical model will be effective with real data this time. Therefore, the primary objective of this project is to achieve material discrimination and identification in laboratory XCT systems. This involves finding ways to quantitatively extract information from materials, such as their atomic numbers, as well as working on reconstruction algorithms to account for beam-hardening artifacts.

This work focuses on investigating X-ray attenuation models that are based on the principle of the multi-energy imaging method. In this project, I aim to explore both simulations and experiments using the existing model and the proposed model, to demonstrate the reduction of beam-hardening artifacts visually and to obtain quantitative measurements that enable material identification.

The thesis proceeds as follows: Chapter 2 introduces the X-ray spectrum generation process and relevant X-ray attenuation mechanisms and their models. Chapter 3 illustrates more details and limitations of approaches to reduce beam-hardening artifacts as mentioned in Section 1.4, and delves deeper into the mathematical details of the models for multi-energy imaging, including the existing attenuation model and the proposed model. Chapter 4 introduces the noise model in X-ray measurements and the method for estimating the mean energy of the X-ray spectrum. Chapter 5 describes the simulation processes, and the results from different models are compared both visually and quantitatively. Chapter 6 illustrates the experimental calibration procedures for implementing the proposed model. Chapter 7 describes the experimental process, with results discussed both visually and quantitatively, and compared to theoretical predictions. The findings from Chapters 5, 6, and 7 are summarised in Chapter 8, where an outlook on potential future work is also provided.

Chapter 2

Background theory Part 1: X-ray/Matter Interactions

In this chapter, I introduce the fundamentals of X-ray physics, including how X-rays are generated, as well as X-ray attenuation mechanisms and their relevant models. This lays the foundation for understanding the interaction of X-rays with matter, which is pivotal in quantitative XCT, as it helps us comprehend the underlying processes and identify the sources of uncertainties that might be encountered in experiments.

2.1 X-ray Spectrum Generation

X-rays are produced within the X-ray source, also known as an X-ray tube (see Figure 2.1). It is equipped with a filament cathode and a metallic anode (or target). When a high voltage is applied between these electrodes, electrons from the cathode are rapidly accelerated. As these high-velocity electrons strike the metal anode, they decelerate or come to a sudden stop. This abrupt deceleration causes the electrons to release energy in the form of X-rays [23]. Common materials for the target include tungsten, molybdenum, and copper. The choice of anode material can influence the reflection and transmission types of the X-rays produced [23]. For instance, tungsten, with its high atomic number, is effective in producing high-energy X-rays more commonly used in materials science and geology [24]. On the other hand, molybdenum, with its lower atomic number, produces softer X-rays [24]. These are often used to image less attenuating elements that are more prevalent in life science and biological imaging.

The X-ray spectrum generated in an X-ray tube primarily consists of two components:

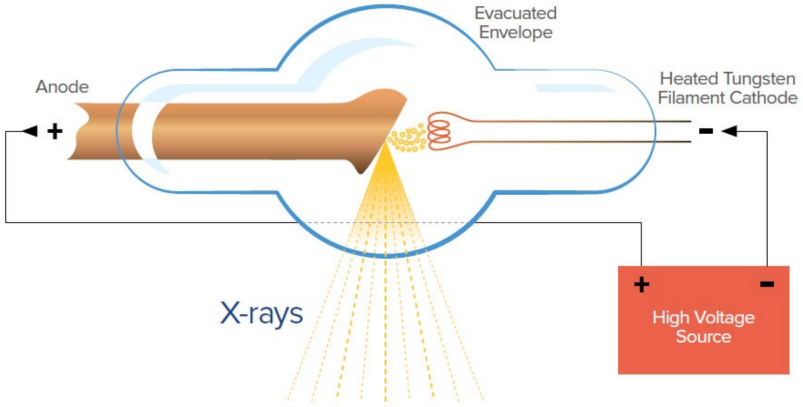

Figure 2.1: Schematic of a reflection target X-ray tube. X-rays are produced when high-energy electrons strike the metal anode. [23]

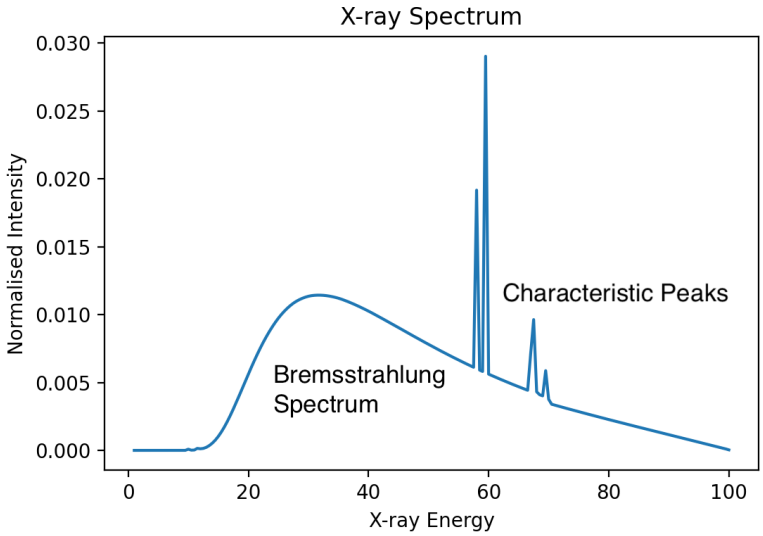

Figure 2.2: A typical X-ray spectrum that consists of Bremsstrahlung and characteristic peaks.

a continuous and smooth curve, and peaks (see Figure 2.2). The continuous spectrum, known as 'Bremsstrahlung', a German term meaning 'braking radiation', is the X-ray radiation produced when high-energy electrons are decelerated by the nuclei of atoms in the target material of the X-ray tube [25]. The energy reduction of the electrons manifests as X-ray photons, yielding a continuous spectrum [23]. The maximum energy of the produced X-ray equals the energy of the incident electrons, which is determined by the voltage applied across the X-ray tube.

The peaks are called characteristic peaks. When the incident electrons have enough energy, they can knock out inner-shell electrons from the target atoms. When electrons

from higher energy levels fall into these inner-shell vacancies, the energy difference between the two shells is emitted as X-ray radiation with specific energies [25]. These emissions are termed 'characteristic' because they have distinct, well-defined energies unique to the target material [23].

2.2 Relevant X-ray Attenuation Mechanisms and Their Models

In the typical imaging energy range of 10 to 120 keV, X-rays interact with matter and attenuate primarily through three mechanisms (shown graphically in Figure 2.3):

1. **Photoelectric Absorption (PE):**

   In this process, an X-ray photon interacts with an inner-shell electron of an atom, completely absorbing the photon's energy and ejecting the electron from its shell [26]. The inner-shell electrons of an atom are organized into various shells, known as K, L, M shells, and so on [27]. The K-shell, closest to the nucleus, has the highest binding energy, followed by the L and M shells. When an X-ray photon's energy exceeds the binding energy of an electron in one of these shells, it can eject that electron, creating a vacancy. This ejected electron is termed a photoelectron [26]. This vacancy is often filled by an electron from a higher shell, emitting energy in the form of a characteristic X-ray. PE dominates at lower energies, typically less than 30 keV [13].

2. **Compton Scattering (CS):**

   Compton (or inelastic/incoherent) scattering occurs when an X-ray photon interacts with a loosely-bound outer electron of an atom. The photon transfers a portion of its energy to the electron, ejecting it, and the photon is deflected from its original path [26]. The scattered photon has reduced energy compared to the incident photon [13]. CS becomes more prominent (relative to PE) at higher energies [13].

3. **Rayleigh Scattering (RS):**

Rayleigh (or elastic/coherent) scattering is a process in which X-rays interact with an atom, resulting in the scattering of the X-ray photon without any energy loss, but with a change in direction [13]. Rayleigh scattering causes refraction, and while this effect is very small, it allows for phase-contrast X-ray imaging. However, when compared to PE and CS, its effect on the X-ray attenuation coefficient of interest is negligible.

Figure 2.3 shows the total mass attenuation coefficient of aluminum and copper as examples, composed of PE, incoherent scattering (CS), and coherent scattering (RS) components. All materials exhibit a similar trend in the attenuation coefficient curve, with PE dominating at lower energies and CS at higher energies. Note that the sudden jump in PE attenuation (at between 10^{-3} and 10^{-2} MeV in the plots) is called the K-edge discontinuity.

2.2.1 Beer-Lambert Law and Attenuation Coefficient Model

The Beer-Lambert Law relates the attenuation of monochromatic radiation to the line integral of the attenuation coefficient, μ, as:

$$\mu l = -\ln\left(\frac{I}{I_0}\right), \tag{2.1}$$

where l represents the distance that the X-ray beam travels through the object, I_0 is the intensity of the incident beam, and I is the intensity of the transmitted beam.

Since X-ray sources are polychromatic, the attenuation coefficient μ is a function of energy E, the Beer-Lambert Law can be adapted to account for that, yielding the transmitted intensity as:

$$I = I_0 \int_0^{E_{max}} S(E) e^{-\mu(E)\cdot l} dE, \tag{2.2}$$

where $S(E)$ is the normalised incident X-ray spectrum generated by the X-ray source with E_{max} equals the energy of the incident electron.

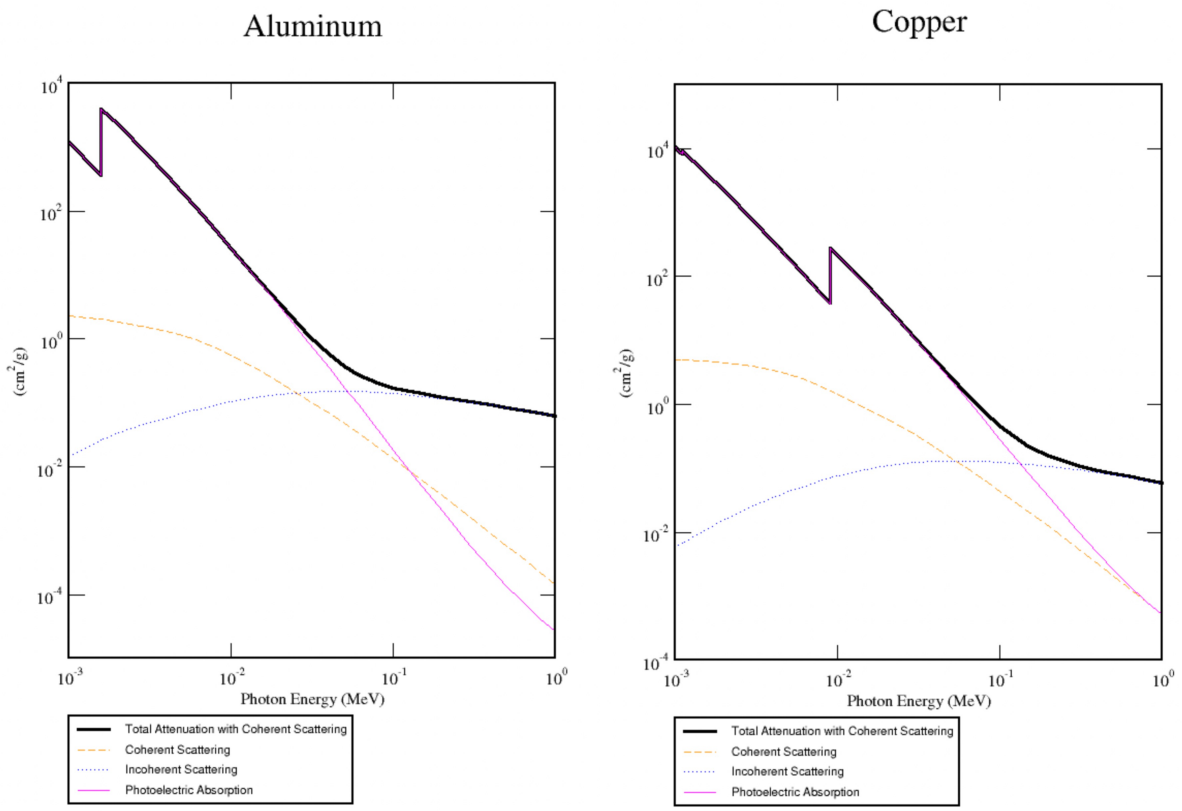

Figure 2.3: Total mass attenuation coefficient of aluminum (left) and copper (right), composed of photoelectric absorption, incoherent scattering (Compton scattering), and coherent scattering (Rayleigh scattering). Note that the sudden jump at very low energy is called the K-edge discontinuity. (Image generated using data from NIST.XCOM [28])

2.2.2 Alvarez and Macovski (AM) Attenuation Model

Alvarez and Macovski demonstrated that the X-ray attenuation coefficient (for $\sim 10-500$ keV) for a material, $\mu(E)$, can be approximately modeled by a relatively simple function that is an energy-dependent linear combination of PE and CS [21]. In Equation 2.3, function $1/E^m$ approximates the energy dependence of the PE component, where m typically ranges between 3 and 3.5 [13]; and function $f_{KN}(E)$ represents the energy dependence of the total cross-section for the CS component [21]. Therefore, Equation 2.3 is referred to as the AM attenuation model.

$$\mu(E) = a_1 \cdot \frac{1}{E^m} + a_2 \cdot f_{KN}(E), \tag{2.3}$$

where a_1 and a_2 are energy-dependent coefficients discussed below, and $f_{KN}(E)$ is the Klein-Nishina function given by

$$f_{KN}(E) = \frac{1+\alpha}{\alpha^2}\left[\frac{2(1+\alpha)}{1+2\alpha} - \frac{1}{\alpha}\ln(1+2\alpha)\right] + \frac{1}{2\alpha}\ln(1+2\alpha) - \frac{1+3\alpha}{(1+2\alpha)^2}; \alpha = \frac{E}{m_e c^2}, \tag{2.4}$$

where m_e is the electron mass, $m_e c^2 \approx 511$ keV.

The dependence of a_1 and a_2 on the material's inherent physical parameters is as follows:

$$a_1 \approx K_1 \frac{Z}{A}\rho Z^{n-1}; a_2 \approx K_2 \frac{Z}{A}\rho, \tag{2.5}$$

where K_1 and K_2 are constants, ρ is mass density, A is atomic weight and Z is atomic number.

Equation 2.5 illustrates how the photoelectric absorption and Compton scatter vary with ρ and Z of a material. For PE, the coefficient a_1, the probability of photoelectric absorption occurring is approximately proportional to the cube of the atomic number ($n - 1 \approx 3$) of the attenuating material; for the Compton scattering, the coefficient a_2, is approximately proportional to the number of electrons present [13]. Note that the AM model captures the attenuation in Figure 2.3 accurately for energies above 10^{-2} MeV.

2.2.3 NIST Attenuation Model

The National Institute of Standards and Technology (NIST) provides a comprehensive set of online databases on material properties, including an attenuation coefficient database for a variety of materials. The NIST attenuation model provides energy-dependent mass attenuation coefficients for photons in materials [28]. This data ranges from low-energy X-rays to high-energy gamma rays. The materials covered in the database span from elements to compounds and even some mixtures. NIST scientists use theoretical models based on quantum mechanics and atomic physics to predict and explain how X-rays and gamma rays interact with matter at the atomic and subatomic level. The dataset is constructed based on a mix of experimental data from the literature and theoretical calculations, often validated against experimental results.

In this work, I will frequently use the attenuation model from NIST X-Ray Cross

Sections Database (NIST.XCOM) [28] as the ground truth data for comparison against other models. Figure 2.4 shows the modeled attenuation for aluminum (Al) and copper (Cu) using the AM model and the NIST model, respectively. The parameters K_1, K_2, m, and n for the AM model are retrieved from [13]. It is important to note that the AM model produces smooth curves, which means it does not properly account for absorption edges (such as the K-edge discontinuity at around 8.98 keV for Cu) [29].

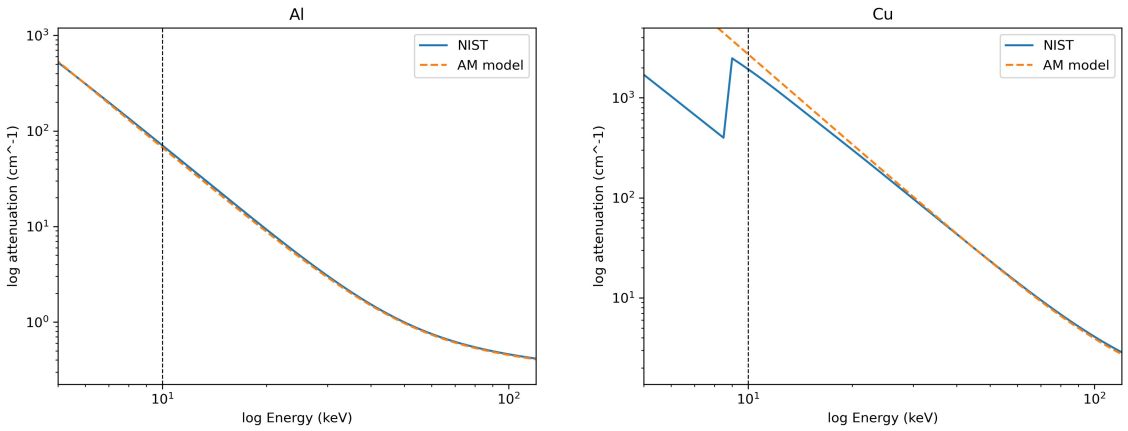

Figure 2.4: Attenuation coefficient curves from 5 to 120 keV for Al and Cu, modeled by the AM model vs. the NIST model.

To summarise, in this chapter, we have learned the fundamental physics of how X-rays are produced and how they interact with matter, as well as the relevant X-ray attenuation models. This chapter lays the foundation to discuss approaches to mitigate the beam-hardening artifacts mentioned in Section 1.4, which I will do in the next chapter.

Chapter 3

Background Theory Part 2: Quantitative X-ray Imaging - Approaches and Limitations

In this chapter, I delve more deeply into the approaches that mitigate the beam-hardening artifacts mentioned in Section 1.4, along with their limitations. Since this work focuses on achieving quantitative XCT using the multi-energy imaging method, I also detail some related models and the underlying mathematics.

3.1 Basic Approaches: Beam Filtration and Linearisation

In this section, I illustrate the basic hardware (beam-filtration) and software (linearisation) approaches to reduce the beam-hardening artifacts. These are probably the most straightforward approaches that one might immediately consider. Here, I explain the principles as well as outline their limitations to emphasise that further improvements to account for beam-hardening are necessary.

Beam Filtration: Beam filtration refers to the 'pre-hardening' process of modifying the incident X-ray beam spectrum. This is achieved by placing specific filters, made of uniform material, in the path between the X-ray tube and the object being imaged (or can be placed after the object too). Figure 1.2 illustrates the spectrum after passing through filters of different thicknesses of Aluminum, resulting in a shift to higher average energy. The purpose of these filters is to reduce low-energy photons, which are undesirable

because they are preferentially absorbed in the object being imaged, thus causing extra beam-hardening artifacts in the reconstructed images [11]. By removing them, these artifacts are mitigated.

However, this method also reduces the number of hard X-ray photons and reduces the signal-to-noise ratio due to increased shot noise. Since the electron beam power in the X-ray tube is limited to prevent damage to the target material that produces the X-rays, the number of X-rays produced can only be increased so far. Adding a filter can then lead to a loss of contrast (higher energy X-rays provide less contrast) and result in more Poisson noise (see Chapter 4 for noise model).

Linearisation: Linearisation in XCT is the process of converting the measured X-ray attenuation values into equivalent 'ideal' values that would be obtained if a monoenergetic X-ray beam were used for a particular reference material. These attenuation values essentially represent a logarithmic depiction of the reduction in X-ray beam intensity due to absorption and scattering within the object. However, because of the polychromatic nature of X-ray sources, these values might not always be inherently linear. This process transforms them into linear coefficients, which are directly related to the density and atomic composition of the materials within the scanned object. Figure 3.1 shows the linearisation curves generated by a direct polynomial fit and other modelling methods, including calibration curves derived from aluminum (Al) step wedges, applied to the measured polychromatic attenuation values.

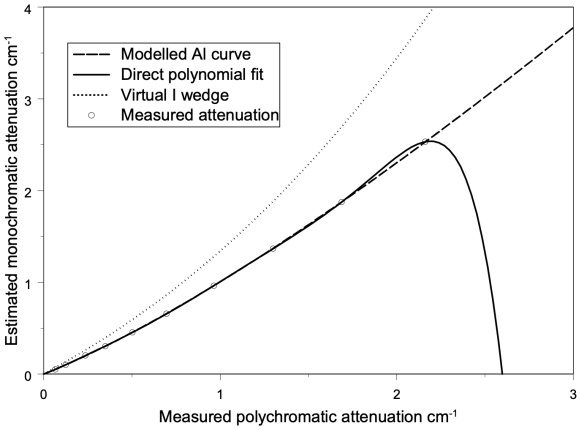

Figure 3.1: Linearisation curves generated through direct polynomial fitting to attenuation measurements, and through other modeling techniques [20].

This method often relies on a calibration curve derived from the known reference material. However, since each material will require a different linearisation curve and it is only effective for single-material objects of similar composition to the reference material.

3.2 Multi-Energy (Dual-Energy) Imaging

To improve material discrimination and characterisation, numerous methods have been developed over the past few decades, with the most well-known being the multi-energy (or dual-energy) imaging method [21, 30]. In general, XCT scans using a soft incident spectrum exhibit both higher contrast and signal-to-noise ratio but more beam-hardening artifacts. Conversely, using a hard spectrum, XCT scans exhibit fewer beam-hardening artifacts, but have lower contrast and signal-to-noise ratio. Figure 3.2 displays two images of the same object, acquired at low and high energy, respectively. In the low-energy image, there is a higher bone-tissue contrast, whereas the high-energy image exhibits reduced contrast. Multi-energy imaging acquires X-ray images using two different incident energy spectra at two distinct energy levels to make use of the complementary information that images from each spectrum provide.

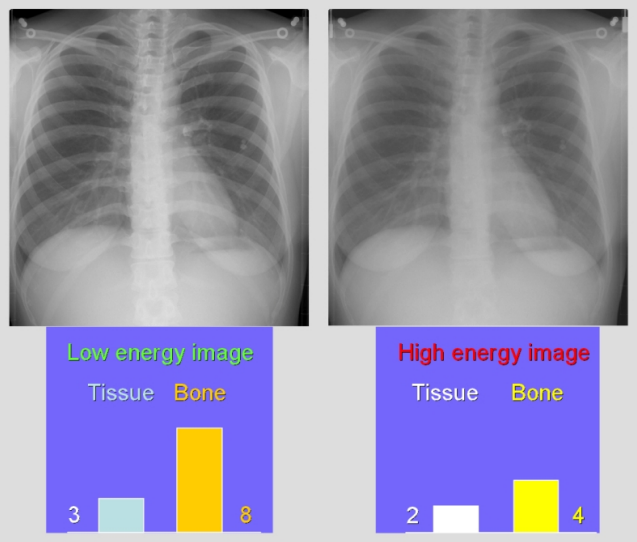

Figure 3.2: Example radiographs of the same object [31], acquired using two distinct X-ray energy beams: one generated with a tube voltage of 60 kVp (green) and the other at 120 kVp (red). An illustration of the relative attenuation of soft tissue and bone is shown below each image, which indicates the difference in attenuation between tissue and bone (contrast) is reduced in the 120 kVp image.

3.2.1 Alvarez and Macovski (AM) Model in Multi-Energy Imaging

The underlying principle of most multi-energy imaging methods is based on the AM model. Here I describe how the AM model enables one to estimate inherent material properties (such as density and atomic number) from projections acquired with two different spectra.

X-ray systems essentially measure the line integrals of the attenuation coefficient: $\int_L \mu(x, y; E) \cdot dl$, where (x, y) represents each pixel location. This is analogous to measuring the line integrals of coefficients a_1 and a_2 as presented in Equation 2.5. From Equation 2.3 we have

$$\mu(x, y; E) = a_1(x, y) \cdot \frac{1}{E^m} + a_2(x, y) \cdot f_{KN}(E), \tag{3.1}$$

where m lies between 3 to 3.5, a_1 and a_2 are inherent properties of the material (i.e., related to density and atomic number) that are independent of energy E, $f_{KN}(E)$ is given by Equation 2.4, then

$$\int_L \mu(x, y; E) \cdot dl = A_1 \frac{1}{E^m} + A_2 f_{KN}(E), \tag{3.2}$$

where

$$A_1 = \int_L a_1(x, y) \cdot dl; \;\; A_2 = \int_L a_2(x, y) \cdot dl. \tag{3.3}$$

Therefore, to reconstruct $a_1(x, y)$ and $a_2(x, y)$, measurements of line integrals A_1 and A_2 are required at every pixel or measurement in the object's projections. To solve the equation with two unknowns, two measurements need to be performed, corresponding to the multi-energy (or essentially multi-spectra) scans. Based on Equation 2.2, the two equations for these measurements can be derived as follows:

$$I_1(A_1, A_2) = I_{01} \int_0^{E_{1max}} S_1(E) e^{[-A_1/E^m - A_2 f_{KN}(E)]} dE \tag{3.4}$$

$$I_2(A_1, A_2) = I_{02} \int_0^{E_{2max}} S_2(E) e^{[-A_1/E^m - A_2 f_{KN}(E)]} dE \tag{3.5}$$

where $S_1(E)$ and $S_2(E)$ are the incident X-ray spectra at different energy levels with I_1 and I_2 the measured total transmitted intensities, I_{01} and I_{02} the corresponding initial incident intensity. E_{1max} and E_{2max} represent the maximum energies of the two incident spectra respectively.

The resolved parameters, A_1 and A_2, at every detector pixel then lead to the reconstruction of $a_1(x, y)$ and $a_2(x, y)$, which reveal the inherent properties of the material (as seen in Equation 2.5). Note that one needs to numerically solve Equations 3.4 and 3.5 for A_1 and A_2 from the measured I_1 and I_2, using two complete spectra. By leveraging the energy-dependent attenuation properties of materials, multi-energy imaging can yield more precise and detailed information about the object's composition. Additionally, because the AM model captures the energy-dependence of the attenuation, it inherently accounts for beam-hardening artifacts. As such, several beam-hardening correction methods have been developed based on this model, either employing its full form [13] or using a simplified version [32]. However, as mentioned earlier in Section 2.2.3, the AM model has limitations: it does not account for K-edge discontinuities and also requires knowledge of effective spectrum information (more details in the next section).

3.2.2 Two-Material (2M) Model in Multi-Energy Imaging

Despite the robust theoretical foundation provided by the AM model for multi-energy imaging, its application is generally constrained by its complexity in the lab. Multi-energy XCT requires more complex hardware and software than single-energy imaging. This includes, for example, perfect alignment between two scans, since minor variations between two measurements might introduce other artifacts that could be difficult to identify. Additionally, the exact form of spectra S_1 and S_2 required in Equation 3.4 and 3.5 is generally very hard to be directly measure and often necessitates a computational fitting process, which includes taking the detector response into account. Hence, multi-energy imaging currently only has niche applications, as no one has yet overcome all the obstacles for its general use.

The two-material (2M) model [33] postulates that X-ray attenuation for a material can be modeled as a linear combination of the attenuations of two known materials,

termed basis materials:

$$\mu(x, y; E) \simeq b_1(x, y) \cdot \mu_1(E) + b_2(x, y) \cdot \mu_2(E), \tag{3.6}$$

where $\mu_1(E)$ and $\mu_2(E)$ are the energy-dependent attenuation coefficients of the known basis materials, and $b_1(x, y)$ and $b_2(x, y)$ are scalars representing their contribution to the total attenuation coefficient. Note that this equation is exact when the attenuation is modeled by the AM model, i.e., the AM model implies the 2M model.

Then in projection space, the basis material line-intergals are given by

$$B_1 = \int_L b_1(x, y) \cdot dl; \;\; B_2 = \int_L b_2(x, y) \cdot dl. \tag{3.7}$$

Similarly, the two equations needed to solve for the two unknowns are given by:

$$I_1(B_1, B_2) = I_{01} \int_0^{E_{1max}} S_1(E) e^{[-B_1 \cdot \mu_1(E) - B_2 \cdot \mu_2(E)]} dE \tag{3.8}$$

$$I_2(B_1, B_2) = I_{02} \int_0^{E_{2max}} S_2(E) e^{[-B_1 \cdot \mu_1(E) - B_2 \cdot \mu_2(E)]} dE \tag{3.9}$$

where $S_1(E)$ and $S_2(E)$ are, as before, the incident X-ray spectra at different energy levels with I_1 and I_2 the measured total transmitted intensities, I_{01} and I_{02} the corresponding initial incident intensity. E_{1max} and E_{2max} represent the maximum energies of the two incident spectra respectively.

The resolved parameters B_1 and B_2 at every pixel of the detector can then be used to reconstruct $b_1(x, y)$ and $b_2(x, y)$, the volume fractions of the basis materials of the target object. If the AM model is assumed, the inherent properties of the target object can then be extracted as the effective electron density and the effective atomic number.

For a composite material, the AM model gives the electron density as

$$\rho_e = \rho \cdot \frac{\sum p_i Z_i}{\sum p_i A_i} \cdot \frac{1}{1\,\mathrm{u}}, \tag{3.10}$$

where ρ is mass density of the material, p_i represents the weights of the number fraction of atom i, Z_i is the atomic number of atom i, A_i is the atomic mass of atom i, and 1 u is 1 atomic mass unit.

Based on [34] and the AM model, the effective atomic number of a material is given by

$$Z_{eff} = \sqrt[3.0]{\sum w_i \cdot Z_i^{3.0}}, \tag{3.11}$$

where w_i the weights account for the contribution to a mixture by element i with corresponding atomic number Z_i.

Therefore, the effective electron density of the target material at every point can be calculated by weighting the volume fractions of the basis materials as:

$$\rho_{e,eff}(x,y) = b_1(x,y) \cdot \rho_{e,1} + b_2(x,y) \cdot \rho_{e,2}, \tag{3.12}$$

where $\rho_{e,1}$ and $\rho_{e,2}$ are electron densities of basis material 1 and 2.

Using Equation 3.11, the effective atomic number at every point of the target material can be calculated as:

$$Z_{eff}(x,y) = \sqrt[3.0]{w_1(x,y) \cdot Z_1^{3.0} + w_2(x,y) \cdot Z_2^{3.0}}, \tag{3.13}$$

where Z_1 and Z_2 are the atomic numbers of the basis materials, $w_{1,2}$ are the mass fractions of basis material 1 and 2:

$$w_i = \frac{b_i(x,y) \cdot \rho_i}{b_1(x,y) \cdot \rho_1 + b_2(x,y) \cdot \rho_2}, \tag{3.14}$$

where ρ_1 and ρ_2 are mass densities of the basis material 1 and 2 respectively.

Equations 3.8 and 3.9 can be applied in the same way as the AM model, i.e., Equations 3.4 and 3.5; it is possible to computationally fit spectra S_1 and S_2 to solve these equations. Another approach, which does not necessitate full spectrum knowledge, is simply making measurements of X-ray attenuation for different basis materials combinations to approximate where the target material fits in. This approach has the potential to simplify laboratory XCT calibration and will be further explored in Chapter 6.

3.3 Hyperspectral Imaging

Hyperspectral imaging captures full spectral data per detector pixel to identify materials and features in images [22]. In traditional single-energy or multi-energy imaging, an energy-integrating detector is employed. This integrates the energy of all detected photons at each pixel. In contrast, hyperspectral imaging employs a 'photon-counting' energy-dispersive detector that measures the photon energy of each arriving X-ray separately and constructs a spectrum for each pixel. This introduces a spectral dimension alongside the spatial dimensions, enabling discrimination between materials with similar grayscale levels by analyzing variations in their absorbed X-ray spectra.

However, it is important to note that photon-counting detectors can only detect a limited number of photons per second, making this method time-consuming because each photon needs to be recorded separately, and the technology currently lacks the energy resolution precision required for accurate material identification across a wide range of elements and energies. Furthermore, the advantage of discriminating between a small range of elements usually does not justify the increased cost of these specialized detectors, which can reach up to $2 million, approximately twenty times the cost of conventional detectors. Overall, this technique, while promising, is not yet mature in practice.

In summary, in this chapter, we have learned the working principles of multi-energy imaging and understand how this method can enable quantitative XCT, which is the objective of this work. We have illustrated the AM and 2M models, which will be the two models of focus throughout this work. In the next chapter, I will introduce X-ray photon statistics, which is crucial for understanding noise in X-ray images.

Chapter 4

Background Theory Part 3: X-ray Photon Statistics and Noise

In this chapter, I introduce the noise model used in this work, which will be employed in simulating X-ray measurements in the next chapter. This model also provides the method for estimating the mean energy of the X-ray spectrum being detected, which is also included in this chapter.

4.1 Noise Model

In X-ray measurements, noise models are of paramount importance for statistical image reconstruction, particularly in the context of low-dose scans and the execution of realistic simulations [35, 36]. While the statistical phenomena related to X-ray measurements are very complex in nature [37], in practical applications, certain simple approximations, such as the Poisson & Gaussian model [36], are sufficient. Consequently, in XCT, we primarily consider two types of noise, which are as follows:

1. **Photon Shot Noise**

   Photon shot noise occurs because photons arrive at a detector in a random and unpredictable manner, reflecting the quantum nature of light [38]. Assuming that the photons are uncorrelated, the number of emitted photons follows a Poisson distribution for a given tube current [36]. If the number of transmitted photons is denoted as N with a mean value $\bar{N}$ proportional to the current, the probability

density distribution of which follows:

$$N \sim \text{Poisson}(N),\ \text{i.e.},\ P(N=k) = \frac{\bar{N}^k e^{-\bar{N}}}{k!},\ k = 0, 1, 2, ... \tag{4.1}$$

where the mean value $\bar{N}$ also equals to the variance of N.

2. **Electronic Noise**

   Electronic noise arises from various sources within electronic components, such as photosensors and preamplifiers, and can manifest as voltage or current variations that are not part of the intended signal [39]. One reasonable model for this noise is a Gaussian distribution. Assuming we have a signal x with a noise-free mean value $\bar{x}$, with Gaussian noise of σ standard deviation, the probability density distribution follows:

$$\text{Gaussian}(\bar{x}, \sigma),\ \text{i.e.},\ P(x) = \frac{1}{\sqrt{2\pi\sigma^2}} \cdot e^{-\frac{(x-\bar{x})^2}{2\sigma^2}}, \tag{4.2}$$

   where we take the electrical signal to be in photon units so that σ is a number of photons.

4.2 Estimating Mean Spectrum Energy: Variance-Mean Ratio

Common X-ray detectors are energy-integrating, i.e., the total energy of the X-rays detected is recorded as opposed to the number of X-rays. In the following discussion, we assume a Poisson distribution model for photon shot noise, i.e., assuming that electronic noise is insignificant relative to photon shot noise.

In monochromatic radiation, assuming we have a mean of N photons detected with energy E, then the measured value in each pixel is given by $I = NE\gamma$, where γ is a detector-dependent parameter that includes detection efficiency and electronic gain [40]. It has recently been realised that, even with an energy-integrating detector, it is possible to get information about the beam spectrum by capturing multiple repeat X-ray images [40]. Assuming a Poisson distribution, the mean value $\bar{N}$ equals to the variance of N, so the standard deviation in the number of photons is given by $\sigma_p = \sqrt{N}$, and the

corresponding standard deviation in intensity is given by $\sigma = \sqrt{N}E\gamma$, and so the intensity variance $\sigma^2 = NE^2\gamma^2$ [40]. Therefore, the X-ray photon energy E as seen by the detector can be calculated by the ratio of the variance and mean intensity: $\sigma^2/I = E\gamma$.

Extending to polychromatic radiation, and assuming γ is not a function of energy, we have a realistic broadband X-ray spectrum, $S(E)$, with $S(E) = E \cdot N(E)$ representing the energy-weighted spectrum. We have $I = \int S(E)\gamma \, dE$, and thus $\sigma^2 = \int S(E)E\gamma^2 \, dE$. Therefore, taking the ratio of the variance to the mean intensity yields the mean energy of the spectrum, denoted as $\langle E \rangle$, as observed by the detector:

$$\frac{\sigma^2}{I} = \frac{\gamma^2 \int S(E)E \, dE}{\gamma \int S(E) \, dE} = \gamma \langle E \rangle . \tag{4.3}$$

The estimation of the mean spectrum energy provides spectral information and essentially measures the amount of beam-hardening (how much the mean energy increases when passing through increasing amounts of material). Hence, it can be used for direct correction of beam-hardening, e.g., fitting with a beam-hardening correction model and finding parameters automatically.

Furthermore, it is found that variance data can be used analogously to mean data in XCT: it will resemble the mean data but be imaged with a harder spectrum (averaging a higher energy) [41]. Therefore, within a single measurement, both mean and variance data can offer equivalent information to the low- and high-energy measurements in multi-energy imaging. Note that this has only been validated through simulation to date.

In conclusion, in this chapter, we have learned about the noise model, that will be applied in simulation, as well as the method for estimating the mean energy of the spectrum being detected using energy-integrating detectors. We now have all the background knowledge required to understand this work. In the next chapter, I will use simulations of a set of simple imaging scenarios to explore quantitative XCT through the AM and 2M attenuation models.

Chapter 5

Simulations of Tomographic Reconstructions

We have seen the potential benefits of achieving quantitative XCT and have understood its working principles. In this chapter, I use simulation to explore the details of quantitative XCT through the two attenuation models introduced in Chapter 3: (1) the two-material model and (2) the Alvarez-Macovski model. Using simulated test objects with simple configurations (referred to as phantoms), I aim to demonstrate that quantitative measurements can theoretically be obtained through multi-energy imaging with appropriate attenuation models. Additionally, I intend to show that beam-hardening artifacts in tomographically reconstructed images can be effectively reduced compared to conventional single-energy reconstruction.

In the following sections, I will first explain how I simulated the intensities measured at the detector, including the correlation with different incident energy spectra. Subsequently, I will illustrate the method used for image reconstruction. This method is conventional, and I will display some images reconstructed using this method directly from simulated intensities to highlight the presence of beam-hardening artifacts. Finally, I will demonstrate how we can apply the two attenuation models to make quantitative measurements, comparing their resulting performance with each other and with that of conventional reconstruction.

This chapter represents my original work on implementing the two-material model for XCT with polychromatic spectra and comparing the performance of the two-material model with the Alvarez-Macovski model. Note that these two models themselves already exist.

5.1 Simulating Single-Energy Measured Intensities (Forward Projection)

In this section, I illustrate the simulation procedure to obtain single-energy measured intensities at the detector in detail. This is the initial step, as it simulates what would be directly measured at the detector in the lab.

In this work, I focussed on a 2D image phantom, as depicted in Figure 5.1. The phantom represents a 2D cross-section through two 3D cylinders composed of different materials; as a convention I refer to the top-left located circle as 'material 1' and the bottom-right one as 'material 2'. I proceeded to simulate the transmitted X-ray intensities measured at the detector as follows:

1. I described the location of each material using a characteristic 'mask' function that equals one where the sample is present and zero elsewhere in the 2D (x, y) space.

2. I projected the characteristic function for each material separately (essentially summing the values along each row at various angles) to obtain the projected characteristic function (the path length in pixels through the material at each direction and position).

3. I multiplied the path length, or the projected characteristic function, by the corresponding material attenuation coefficient at each X-ray energy and the pixel length (with 1 pixel set to 0.005 cm $\times$ 0.005 cm) to derive the projected attenuation functions at every energy for that material. The attenuation data was sourced from the photon cross sections database by the National Institute of Standards and Technology (NIST-XCOM) [28].

4. I summed the projected attenuation functions for both materials and weighted the values in each energy bin by the normalised X-ray spectrum calculated using Python Spekpy library [42] to obtain the total projected attenuation. According to Equation 2.2, the total measured intensities can be calculated as:

$$I = I_0 \sum_E S(E) e^{-[\mu_1(E)\cdot l_1 + \mu_2(E)\cdot l_2]}, \tag{5.1}$$

where I_0 is the initial intensity of the incident beam, $S(E)$ is the normalised X-ray spectrum, $\mu_1(E)\cdot l_1$ and $\mu_2(E)\cdot l_2$ are the projected attenuation functions of material 1 and 2 provided in Step 3.

Finally, I added Poisson and Gaussian noise to the simulated intensities as described in Chapter 4, with a fixed Gaussian standard deviation $\sigma = 15$ photons and a typical I_0 of 10^6 photons per pixel (ppx) for Poisson noise (unless otherwise stated).

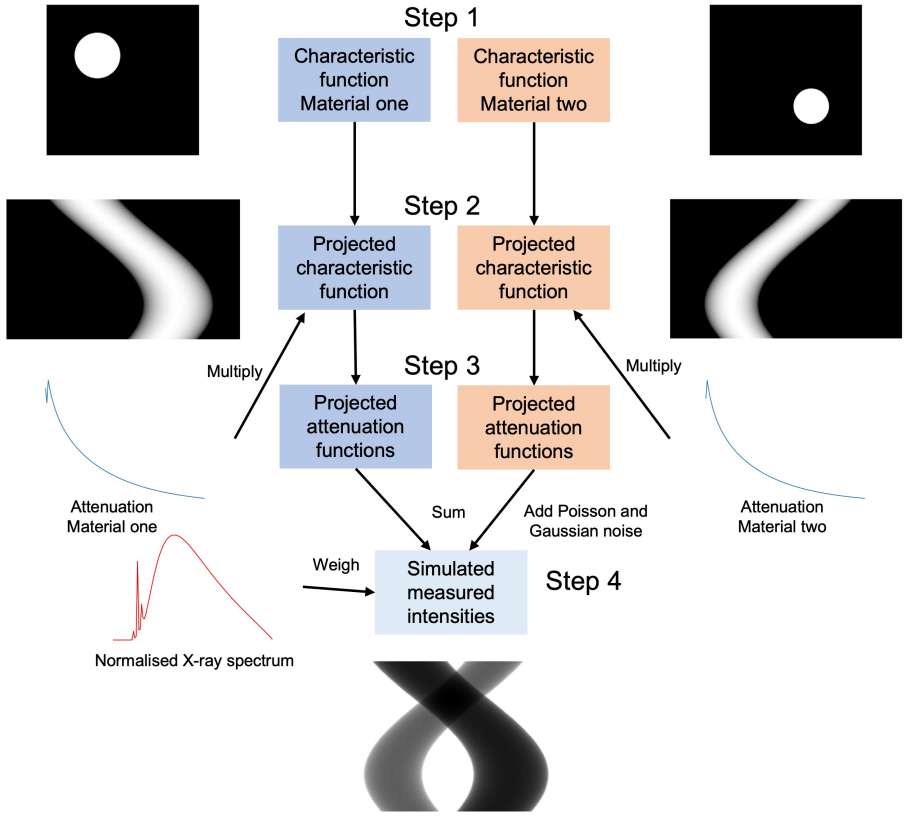

Figure 5.1: Simulating the measured intensities of a phantom consisting of two different materials. Step 1: Using a characteristic function to describe the location of each material. Step 2: The characteristic function for each material is projected separately to determine path lengths. Step 3: The projected characteristic function for each material is multiplied by the corresponding attenuation coefficient at each energy and the pixel size to obtain the projected attenuation at every energy for that material. Step 4: The projected attenuation functions for these two materials are added together and weighted by the normalised X-ray spectrum to give the total measured intensities (Equation 5.1). Poisson and Gaussian noise are added to each energy bin separately.

5.2 Simulating Multi-Energy Imaging

Having seen the simulation process for single-energy imaging, in this section, I illustrate how I simulated multi-energy imaging using that method in this project.

Recall that multi-energy imaging acquires X-ray images using two or more different incident energy spectra at two or more different tube accelerating voltages. The two normalised spectra I here used are illustrated in Figure 5.2. These spectra were simulated using the Python Spekpy library [42]. The low-energy spectrum, $S_1(E)$, was generated with a tube voltage of 60 kV and a 0.5 mm Aluminum (Al) filter, while the high-energy spectrum, $S_2(E)$, was generated with a tube voltage of 120 kV and a 0.35 mm Copper (Cu) filter. Both spectra were normalised so that their integrals (areas under the curve) equaled one.

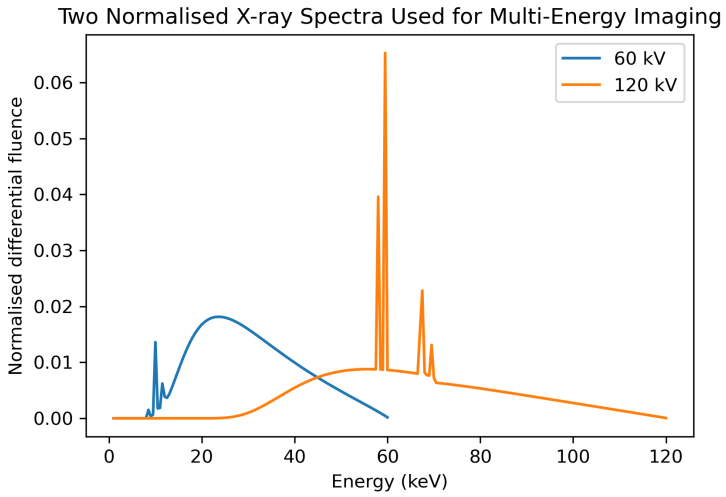

Figure 5.2: Two normalised spectra used in the simulation. The low-energy spectrum is generated at 60 kV with 0.5 mm Al filter (blue). The high-energy spectrum is generated at 120 kV with 0.35 mm Cu filter (orange).

Given these spectra, I used Equation 5.1 to simulate the total measured intensities transmitted – the projections – as follows:

$$I_1 = I_0 \sum_E S_1(E) e^{-[\mu_1(E)\cdot l_1 + \mu_2(E)\cdot l_2]}, \tag{5.2}$$

$$I_2 = I_0 \sum_E S_2(E) e^{-[\mu_1(E)\cdot l_1 + \mu_2(E)\cdot l_2]}. \tag{5.3}$$

Here the initial intensity, I_0, is set to 10^6 ppx (unless otherwise stated), $\mu_1(E) \cdot l_1$ and $\mu_2(E) \cdot l_2$ are the projected attenuation functions of material 1 and 2 contained in the phantom, $S_1(E)$ and $S_2(E)$ are normalised spectra such that $\sum_E S_i(E) = 1$, $i = 1, 2$.

Note that we only need to project materials once to obtain l_1 and l_2 (as illustrated in Step 2 of Figure 5.1), and then combine them with different μ_1 and μ_2 values at different energies from each spectrum.

5.3 Tomographic Reconstruction by Filtered Back Projection

In previous sections, I illustrated how I simulated the forward projection process to obtain the intensities measured at the detector. In this section, I introduce the tomographic reconstruction method used to transform these measured intensities into images or tomograms.

Filtered Back Projection (FBP) is a conventional, analytical image reconstruction technique where one-dimensional projections are used to reconstruct two-dimensional images. These projections are acquired from various angles around an object, creating a sinogram (Step 2 of Figure 5.1). In 'Back Projection', the sinogram's data is smeared or 'back projected' across an image matrix, accumulating values to approximate the object's internal structure. While 'Back Projection' (the adjoint operation to projection) provides a basic reconstruction, it results in blurred images. Ramp filtering is applied to the projections prior to 'Back Projection' to produce clearer and more accurate images [43]. In all reconstructions for this work, I utilised the FBP algorithm from the Python skimage.transform.iradon library with a 'ramp' filter.

Figure 5.3 shows attenuation coefficient maps of phantoms composed of various material combinations: (1) aluminum (Al) and copper (Cu), (2) Al and titanium (Ti), (3) Ti and iron (Fe), as well as (4) magnesium (Mg) and zinc (Zn). The reason for these choices will be outlined in the Section 5.4. These maps were generated from conventional single-energy imaging, projected by the X-ray spectra, $S_1(E)$ (the low-energy spectra employed in multi-energy imaging). The measured intensities were calculated

using Equation 5.2 and then directly reconstructed using FBP. The corresponding line profiles were generated along the red diagonal lines marked in the images. In these conventional reconstructions, both cupping (circled by green dotted lines, areas that should be flat if there is no beam-hardening) and streaking artifacts (indicated by white arrows, which show unwanted patterns between two materials) were observed at varying degrees. Also, it was not possible to extract quantitative information directly from these images.

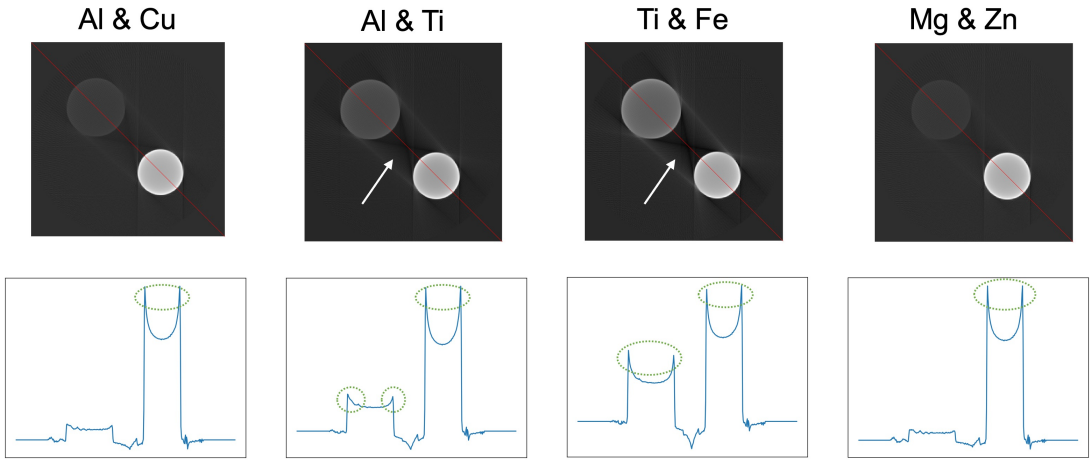

Figure 5.3: Attenuation maps generated from conventional single-energy imaging, projected by the X-ray spectra generated at 60 kV with a 0.5 mm Al filter, and reconstructed using the FBP algorithm. The corresponding line profiles were generated along the red diagonal lines marked in the images. The four phantoms are: (1) Top circle - Al, bottom circle - Cu; (2) Top circle - Al, bottom circle - Ti; (3) Top circle - Ti, bottom circle - Fe; (4) Top circle - Mg, bottom circle - Zn. Note the presence of beam-hardening artifacts, particularly cupping (green dotted circles), and also streaking (white arrows).

In the following sections, I am going to apply both the two-material and the Alvarez-Macovski models to intensity data obtained using two energy spectra, demonstrating that we can extract quantitative information through multi-energy imaging. We will also see that the beam-hardening artifacts present in conventional single-energy imaging can be greatly mitigated using these methods. Furthermore, we will be able to compare the performance and robustness of these two models.

5.4 Two-Material (2M) Model for X-ray Attenuation

In this section, I illustrate the 2M model, detail the simulation process, and present reconstruction results for both visualisation and quantitative measurements. I aim to determine whether beam-hardening is reduced and the precision to which we can extract the quantitative results obtained from this analysis.

5.4.1 Method

According to Section 3.2.2, for this simulation, I selected two common materials: Aluminum (Al) with an atomic number of 13 and Copper (Cu) with an atomic number of 29 as the two basis materials in the proposed 2M model.

I focused on examining four phantoms made up of different combinations of materials:

1. **Al and Cu:** Exactly the same as the two basis materials.
2. **Al and Titanium (Ti):** Al is the same as one of the basis materials, Ti is in between the atomic number range defined by the basis materials.
3. **Ti and Iron (Fe):** Both materials are different from the basis materials, but their atomic numbers fall within the range defined by the basis materials, i.e., the atomic number of Ti is 22, and that of Fe is 26, both within the range provided by Al (13) and Cu (29).
4. **Magnesium (Mg) and Zinc (Zn):** Both materials are different from the basis materials, and their atomic numbers lie outside the range defined by the basis materials. To clarify, the atomic number of Mg is 12, and that of Zn is 30.

Based on Equation 3.8 and 3.9, for each pixel in each measured sinogram we have:

$$I_1 = I_0 \sum_E S_1(E) e^{-[\mu_{Al}(E)\cdot B_{Al} + \mu_{Cu}(E)\cdot B_{Cu}]}, \tag{5.4}$$

$$I_2 = I_0 \sum_E S_2(E) e^{-[\mu_{Al}(E)\cdot B_{Al} + \mu_{Cu}(E)\cdot B_{Cu}]}, \tag{5.5}$$

where $I_{1,2}$ are simulated measured intensities using Equations 5.2 and 5.3 given the materials in the interested phantom, $\mu_{Al}(E)$ and $\mu_{Cu}(E)$ are attenuation coefficients of Al and Cu taken from NIST-XCOM database [28].

The line-integrals B_{Al} and B_{Cu}, which are the unknowns in Equations 5.4 and 5.5, were numerically solved by performing a minimisation of the log-likelihood function (MLE) for given measured total intensities for each pixel [44]. The optimisation method employed was the Limited-memory Broyden-Fletcher-Goldfarb-Shanno with Box constraints (L-BFGS-B) algorithm [45] provided by the Python scipy.optimize.minimize library.

Subsequently, I applied the FBP algorithm to the B_{Al} and B_{Cu} sinograms to reconstruct images of $b_{Al}(x, y)$ and $b_{Cu}(x, y)$. These images illustrate the volume fractions of the basis materials Al and Cu at each pixel. Using Equations 3.12 and 3.13, I then calculated density and atomic number images. I computed the mean values within the regions of interest on these images (where the sample is present) and compared them quantitatively with the actual density and atomic number values.

5.4.2 Results & Discussions

Figure 5.4 illustrates the reconstructed volume fraction maps $b_{Al}(x, y)$ and $b_{Cu}(x, y)$ for the basis materials Al and Cu produced by the 2M model. Figure 5.5 shows density and atomic number maps with corresponding line profiles generated along the red diagonal lines marked in the images, I have also included the theoretical values provided by the NIST-XCOM database [28]. Note that the original reconstructed atomic number maps were distorted by extreme values in the background, (i.e., divisions by extremely small numbers in Equation 3.14), thereby obscuring meaningful features. I deliberately set volume fraction values b_{Al} and b_{Cu} less than 0.05 (within uncertainty, the extremely small values obtained in the background from optimisation that were indistinguishable from zero) to 0 when calculating the atomic number in reconstruction. The mean values of density and atomic number from the regions of interest within the circular areas can then be extracted. The quantitative results were summarised in Table 5.1, where the relative error was calculated in relation to the actual values (the values used in the forward projection when the simulated projections were calculated): the absolute difference

between the actual value and the reconstructed value, divided by the actual value. Note that in this study, I did not explicitly calculate the standard deviation within the areas of interest. This was because the primary objective is the mean value, i.e., the quantitative measurements in regions of interest where we know that a particular region is composed of the same material. The standard deviation indicates the noise level in the reconstructed images and the stability of the reconstruction method, aspects that are not the main focus here.

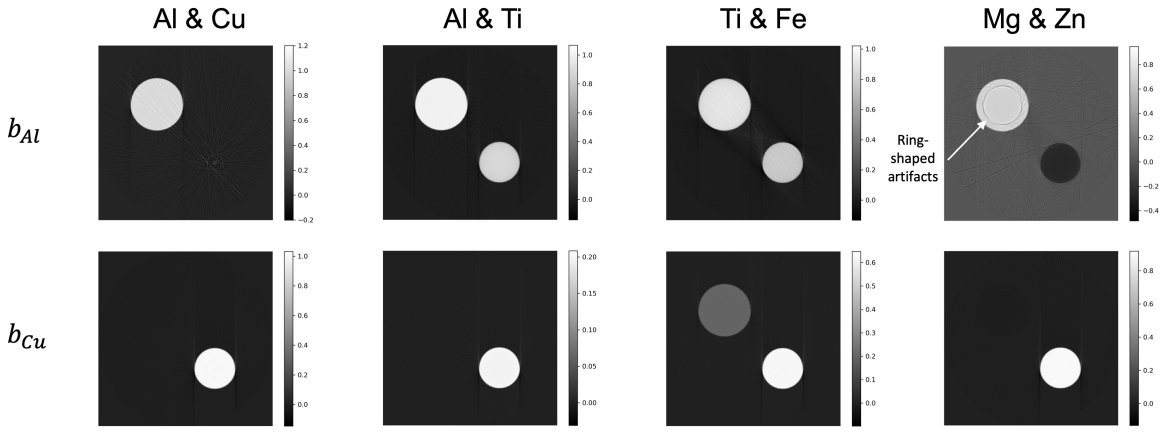

Figure 5.4: Reconstructed volume fractions maps b_{Al}, b_{Cu}, produced by the proposed 2M model using Al and Cu as basis materials. The configurations of the four phantoms are: (1) Top circle - Al, bottom circle - Cu; (2) Top circle - Al, bottom circle - Ti; (3) Top circle - Ti, bottom circle - Fe; (4) Top circle - Mg, bottom circle - Zn.

	ρ (gr/cm^3) (2M)	ρ (gr/cm^3) (GT)	Rel err (ρ)	Z (2M)	Z (GT)	Rel err (Z)
Al	2.704	2.70	0.16 %	12.90	13	0.77 %
Cu	8.957	8.96	0.03 %	28.99	29	0.03 %
Ti	4.095	4.506	9.12 %	22.64	22	2.90 %
Fe	7.661	7.86	2.53 %	26.39	26	1.50 %
Mg	1.820	1.738	4.72 %	13.00	12	8.33 %
Zn	7.320	7.14	2.38 %	29.00	30	3.33 %

Table 5.1: Density (ρ) and atomic number (Z) values reconstructed by the 2M model, averaged over the region of interest in the circular area, compared to theoretical values (GT)

Upon inspecting these maps, one can observe that beam-hardening artifacts (cupping and streaking) were insignificant in most reconstructions, though minor cupping was still observed in atomic number profiles for Al & Ti and Ti & Fe phantoms. The streaking

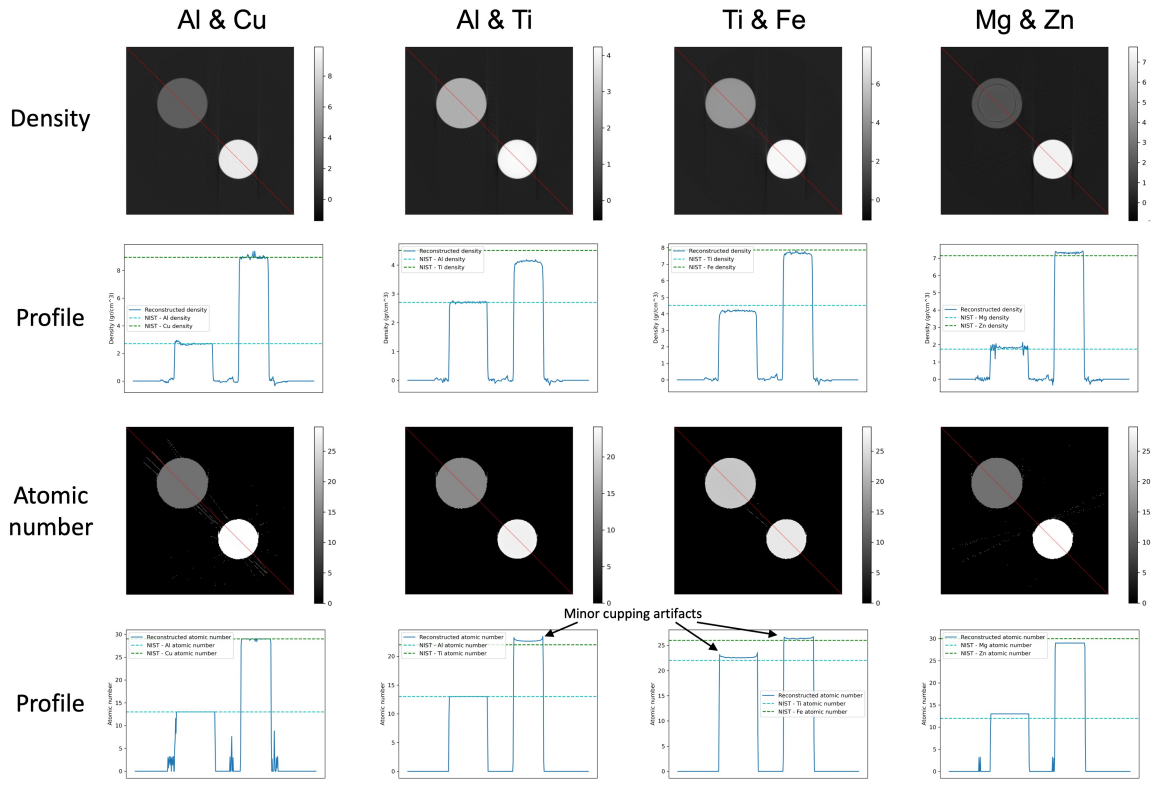

Figure 5.5: Reconstructed density and atomic number maps produced by the 2M model, with corresponding line profiles generated along the red diagonal lines marked in the images. The theoretical values (NIST-XCOM) are given by the cyan and green lines in the profiles. The four phantoms are: (1) Top circle - Al, bottom circle - Cu; (2) Top circle - Al, bottom circle - Ti; (3) Top circle - Ti, bottom circle - Fe; (4) Top circle - Mg, bottom circle - Zn.

lines in the Al & Cu and Ti & Fe phantoms, as well as the ring-shaped artifacts in the Mg & Zn phantom, arose from optimisation failures along those particular lines. A failure to find the optimal solution for B_{Al} and B_{Cu} in Equations 5.4 and 5.5 would result in an incorrect data point in the data set. When back-projecting that data point using FBP (which essentially assigns the same value along a particular line) to reconstruct images, it manifests as an incorrect line (line artifact). I observed that the reconstructed features in the Mg & Zn phantom were the most unstable among all volume fraction reconstructions, containing various artifacts. Furthermore, I noticed negative values in the volume fraction map b_{Al} of the Mg & Zn phantom. This was as expected, since Mg and Zn fall outside the range defined by the basis materials. It is important to note that negative pathlengths are technically challenging to achieve in experiments, as it is not

possible to physically calibrate the 2M model for negative volume fractions of the basis materials.

From the line profiles and quantitative results, it was also observed that the relative errors were minimised for Al and Cu because they were the same as the basis materials and were, therefore, inherently more accurate than other materials. The large error in atomic number and instability in the reconstructed image for Mg primarily arose because its atomic number falls outside the range defined by the basis materials. An intriguing finding was the larger relative error for Ti compared to the results obtained in [33]. This discrepancy might be due to the choice of basis materials. In this study, I selected Cu as one of the basis materials because it has an atomic number of 29, allowing more elements to fall within the range defined by the basis materials, i.e., Z ranging from 13 to 29. However, Cu exhibits a K-edge discontinuity around 8.98 keV (as seen in Figure 2.4), which can complicate the fitting process. This can lead to larger errors in the density and atomic number reconstructions for certain materials.

These observations highlight the complexities of choosing basis materials in practice. A limitation of the 2M model is its inaccuracy for materials whose atomic numbers fall outside the range defined by the basis materials. Opting for a high-atomic-number material as one of the basis materials can expand the range of materials for which we can obtain meaningful results. However, most high-atomic-number materials exhibit a K-edge discontinuity at higher energies ($\geq$ 10 keV), which can significantly impact the fitting process, thereby affecting the accuracy of quantitative results when reconstructing the density and atomic number of materials of interest. Therefore, the selection of basis materials should depend on the approximate range of materials contained in the object of interest (if known). This selection can also be adjusted until reasonable results are obtained.

5.5 Alvarez-Macovski (AM) Model for X-ray Attenuation

In this section, I examine the existing AM model, detail the simulation process which is similar to the 2M model in structure, and also present reconstruction results for both visualisation and quantitative analysis. The results obtained in this section can provide a comparison with the 2M model.

5.5.1 Method

For reconstruction with the AM model (refer to Section 2.2.2 and 3.2.1), I used a set of universal parameters fitted in [13] that work for a wide range of materials: $K_1 = 13.96$ keV^{3}cm^2/gr, $K_2 = 0.30$ cm^2/gr, $m = 3.0$, and $n = 4.2$. Once again, I examined the performance on the same four phantoms of interest as in the 2M model for the purpose of comparison.

I adjusted Equation 3.4 and 3.5 to give:

$$I_1 = I_0 \sum_E S_1(E) e^{-[\mu_{PE}(E)\cdot A_1 + \mu_{CS}(E)\cdot A_2]}, \tag{5.6}$$

$$I_2 = I_0 \sum_E S_2(E) e^{-[\mu_{PE}(E)\cdot A_1 + \mu_{CS}(E)\cdot A_2]}, \tag{5.7}$$

where $I_{1,2}$ are ground truth intensities simulated given the materials in the interested phantom, $\mu_{PE}(E)$ and $\mu_{CS}(E)$ are the photoelectric absorption and Compton scattering components of the attenuation, and are analogous to the material attenuations $\mu_{Al}(E)$ and $\mu_{Cu}(E)$ in the 2M model. The behaviour of $\mu_{PE}(E)$ and $\mu_{CS}(E)$ as a function of energy is as follows:

$$\mu_{PE}(E) = \frac{K_1}{E^m};\ \mu_{CS}(E) = K_2 \cdot f_{KN}(E). \tag{5.8}$$

The sets of line-integrals A_1 and A_2 were numerically solved by minimising the least square error (LSE) based on the given measured total intensities [46]. The optimisation method employed was the Nelder-Mead algorithm [47] provided by the Python

scipy.optimize.minimize library. Subsequently, I applied the FBP algorithm to the A_1 and A_2 sinograms to perform pixelwise tomographic reconstructions of images $a_1(x, y)$ and $a_2(x, y)$. Note that the optimisation methods in both the 2M and AM models (L-BFGS-B and Nelder-Mead, respectively) were chosen based on the optimised values that provided the most robust reconstructed images. As mentioned before, failing to find the minimum could result in a bad pixel value, which would be back-projected, causing a line artifact in the reconstructed images.

According to Equation 2.5, image $a_1(x, y)$ provides the reconstruction map of

$$a_1(x, y) = \frac{\rho(x, y) \cdot Z^n(x, y)}{A(x, y)}, \tag{5.9}$$

while image $a_2(x, y)$ provides the reconstruction map of

$$a_2(x, y) = \frac{\rho(x, y) \cdot Z(x, y)}{A(x, y)}. \tag{5.10}$$

Assuming $A \simeq 2Z$, the density image can be obtained as

$$\rho(x, y) = 2 \cdot a_2(x, y), \tag{5.11}$$

and the atomic number image as

$$Z(x, y) = \left(\frac{a_1(x, y)}{a_2(x, y)}\right)^{\frac{1}{n-1}}. \tag{5.12}$$

note that Equation 5.12 becomes unstable as $a_2(x, y) \to 0$.

Again, I computed the mean values within the regions of interest on these images and compared them quantitatively with the theoretical density and atomic number values.

5.5.2 Results & Discussions

Figure 5.6 illustrates the a_1 and a_2 maps produced by the AM model for the same set of phantoms used in the 2M model (see Figure 5.4). Figure 5.7 shows density and atomic number maps with corresponding line profiles generated along the red diagonal lines marked in the images. Again I have included theoretical values provided by the NIST-

XCOM database [28]. Recall that the reconstructed atomic number maps were distorted by extreme values in the background, (i.e., divisions by extremely small numbers in the a_2 images), making it hard to recognise features in the areas of interest. I deliberately set values in a_2 images less than 0.2 (extremely small values obtained in the background from optimisation) to 0 when calculating the atomic number in reconstruction. The mean values of density and atomic number from the regions of interest within the circular areas can then be extracted. The quantitative results were summarised in Table 5.2, with the error calculated relative to the theoretical values: the absolute difference between the theoretical value and the reconstructed value, divided by the theoretical value.

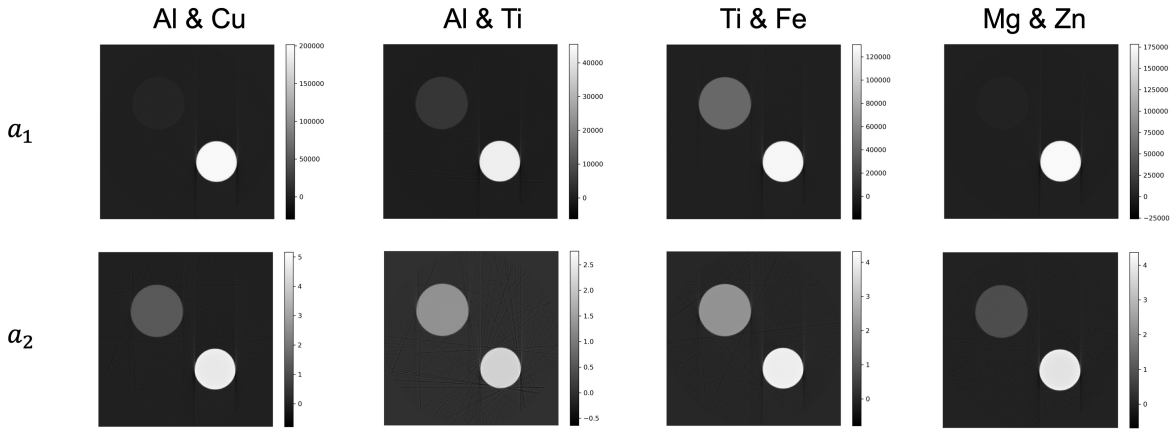

Figure 5.6: Reconstructed a_1 and a_2 maps produced by the AM model. The four phantoms are: (1) Top circle - Al, bottom circle - Cu; (2) Top circle - Al, bottom circle - Ti; (3) Top circle - Ti, bottom circle - Fe; (4) Top circle - Mg, bottom circle - Zn.

	ρ (gr/cm^3) (AM)	ρ (gr/cm^3) (GT)	Rel err (ρ)	Z (AM)	Z (GT)	Rel err (Z)
Al	2.563	2.70	5.07 %	12.94	13	0.46 %
Cu	9.187	8.96	2.53 %	27.69	29	4.52 %
Ti	4.237	4.506	5.97 %	21.81	22	0.86 %
Fe	7.765	7.86	1.21 %	25.42	26	2.23 %
Mg	1.692	1.738	2.65 %	11.35	12	5.42 %
Zn	7.615	7.14	6.65 %	28.28	30	5.73 %

Table 5.2: Density (ρ) and atomic number (Z) values reconstructed by the AM model, averaged over the region of interest in the circular area, compared to theoretical values (GT).

Inspecting these reconstructed maps, it is difficult to observe the presence of beam-hardening, such as cupping or streaking artifacts. As with the multi-energy 2M model,

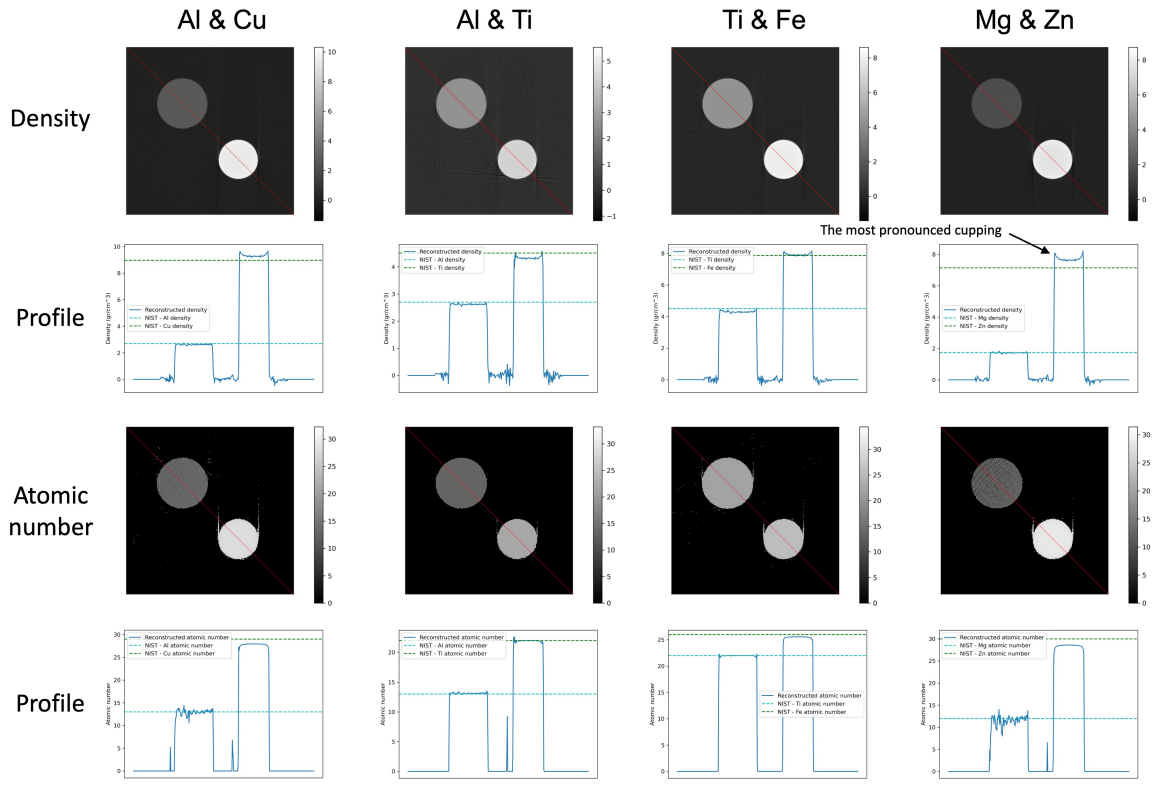

Figure 5.7: Reconstructed density and atomic number maps produced by the AM model, with corresponding line profiles generated along the red diagonal lines marked in the images. The theoretical values (NIST-XCOM) are given by the cyan and green lines in the profiles. The four phantoms are: (1) Top circle - Al, bottom circle - Cu; (2) Top circle - Al, bottom circle - Ti; (3) Top circle - Ti, bottom circle - Fe; (4) Top circle - Mg, bottom circle - Zn.

this highlights the power of multi-energy imaging. Based on the line profiles and quantitative results, the artifacts and errors mainly arose because the AM model does not account for K-edge discontinuities in the PE model. Note that the most pronounced cupping artifacts in the line profiles, as well as the largest relative error, were observed in Zn, which has a K-edge discontinuity at approximately 9.66 keV, the highest among these materials. The relative errors for Al and Mg, which have K-edges at lower energies (Al at 1.56 keV and Mg at 1.30 keV), were higher than expected. While such K-edge discontinuities should minimally affect the model, their elevated errors might be due to the parameters (K_1, K_2, m, and n) for the AM model being universally determined as an average fit for all materials.

5.6 Performance Comparison of the 2M and AM Models

In this section, I compare the performance between the 2M model and the AM model. First, I compare their capabilities in theory by plotting the fitted attenuation coefficients from these two models with the NIST ground truth values. This provides a fundamental understanding of how effective these two models can be. Then, I compare the results obtained by these two models for the four simulated phantoms, consisting of different combinations of materials as illustrated in the previous sections. Finally, I examine the noise sensitivity of these two models.

5.6.1 Method

To gain a fundamental understanding of how well the 2M model compares to the existing AM model, I plotted the attenuation coefficient curves for Al, Cu, Ti, Fe, Mg, and Zn in the energy range of 1 to 120 keV, as provided by the NIST-XCOM database [28] (ground truth), together with the curves fitted by the 2M and AM models, respectively.

The attenuation coefficient curves for all materials fitted using the AM model were determined using Equations 2.3, 2.4, and 2.5, with constant parameters derived from [13].

On the other hand, for the 2M model, the attenuation coefficient curve for each material was fitted individually based on Equation 3.6:

$$\mu(E) = b_1 \cdot \mu_{Al}(E) + b_2 \cdot \mu_{Cu}(E), \tag{5.13}$$

where $\mu_{Al,Cu}(E)$ are attenuation coefficients of basis materials Al and Cu sourced from NIST-XCOM database [28].

I fitted b_1 and b_2 for each material by minimising the sum of the square of the relative errors with respect to the ground truth attenuation values at every energy, i.e., $\min \sum_E \left(\frac{\mu_{NIST}(E)-\mu(E)}{\mu_{NIST}(E)}\right)^2$, from 10 to 120 keV (to avoid K-edge discontinuity in these materials [29]). The optimisation method used was the Nelder-Mead algorithm [47] provided by the Python scipy.optimize.minimize library. As mentioned in Section 5.4, properly modeling negative b_1 and b_2 values in experiments is technically challenging due to the

absence of a suitable model for calibrating negative volume fractions of the basis materials. However, here I allowed negative values as the focus was to examine the fundamental performance of the 2M model in theory.

I calculated the average relative error in the attenuation coefficients for both the AM and 2M models fitted data with respect to the ground truth data as:

$$\frac{\sum_E \left| \frac{\mu_{NIST}(E) - \mu(E)}{\mu_{NIST}(E)} \right|}{N_{bins}}, \tag{5.14}$$

where μ is the attenuation data provided by the AM or 2M model, μ_{NIST} is ground truth attenuation data retrived from NIST.XCOM [28], and the N_{bins} is the total number of energy bins used in generating these attenuation data.

The average relative errors were calculated in the energy range of 10 to 120 keV (the fitting range, which was also the imaging range, as I did not really image with energy less than 10 keV), to quantitatively compare the performance of the 2M and AM models in modeling the attenuation coefficients, which form the basis for image contrast.

I also compared the performance of the 2M model with the AM model in the four simulated phantoms consisting of different combinations of materials as mentioned above by:

1. Visually, I inspected the reconstructed density and atomic number maps generated by these two models to determine whether beam-hardening artifacts were reduced or eliminated compared to the conventional single-energy reconstructions presented in Section 5.3.

2. Quantitatively, I compared the densities and atomic numbers in the circular region of interest reconstructed by both models to the theoretical values.

To compare the noise tolerance of these two models, I selected a phantom consisting of Ti and Fe and introduced increasing levels of noise into the reconstructed density and atomic number images generated by both models. This was achieved by reducing the initial incident intensity in the forward projection process, I_0, from 10^6 ppx to 10^4, 10^3, and even 500 ppx (extremely low), allowing us to assess the sensitivity of these two models to noise.

5.6.2 Results & Discussions

Figure 5.8 shows the attenuation fitted by the 2M and AM models, respectively, and compared with the NIST ground truth attenuation for Al, Cu, Ti, Fe, Mg, and Zn. The corresponding relative error data is summarised in Table 5.3.

Overall, the relative errors of the attenuation fitted by the 2M model were less than those fitted by the AM model when comparing with theoretical values. This was because of the nature that the 2M model assumes a linear combination of attenuations of two basis materials, whereas the AM model fitted data is always a smooth curve. In other words, the 2M model was fitted per plot, while the AM model was fitted on average over all materials. This was also the reason the curves fitted by the AM model showed a large relative error for Cu and Zn. This discrepancy arose because the parameters used for the AM model in [13] were fitted over a range of different materials, but Cu and Zn were outside the atomic number range defined by these materials. The relative errors in the 2M model for Al and Cu were minimised because they were exactly the same as the two basis materials; hence, the fitted curves nearly overlapped with the theoretical curves.

These results provide an understanding of how well the 2M model can potentially perform compared to the existing AM model in theory. However, we should bear in mind that in this fitting process, I had no constraints on the parameters b_1 and b_2 in the linear combination (i.e., they were free to become negative), which led to decent results for materials outside the range defined by the basis materials, namely Mg and Zn.

	Al	Cu	Ti	Fe	Mg	Zn
10 - 120 keV (AM)	2.57 %	5.36 %	3.48 %	4.33 %	2.34 %	5.83 %
10 - 120 keV (2M)	1.06×10^{-3} %	1.41×10^{-4} %	1.68 %	0.84 %	0.97 %	0.35 %

Table 5.3: Average relative error of the fitted attenuation with respect to the NIST ground truth.

In the reconstructions of four simulated phantoms, the 2M model (in Figure 5.5) demonstrated the potential to reduce beam-hardening artifacts and obtain quantitative results comparable to those of the AM model (in Figure 5.7), given the appropriate choice of basis materials. From the line profiles, it was hard to observe any cupping artifacts in the 2M model reconstructions, while cupping artifacts were still visible in the AM model reconstructions for high atomic number materials. From the quantitative results, the 2M

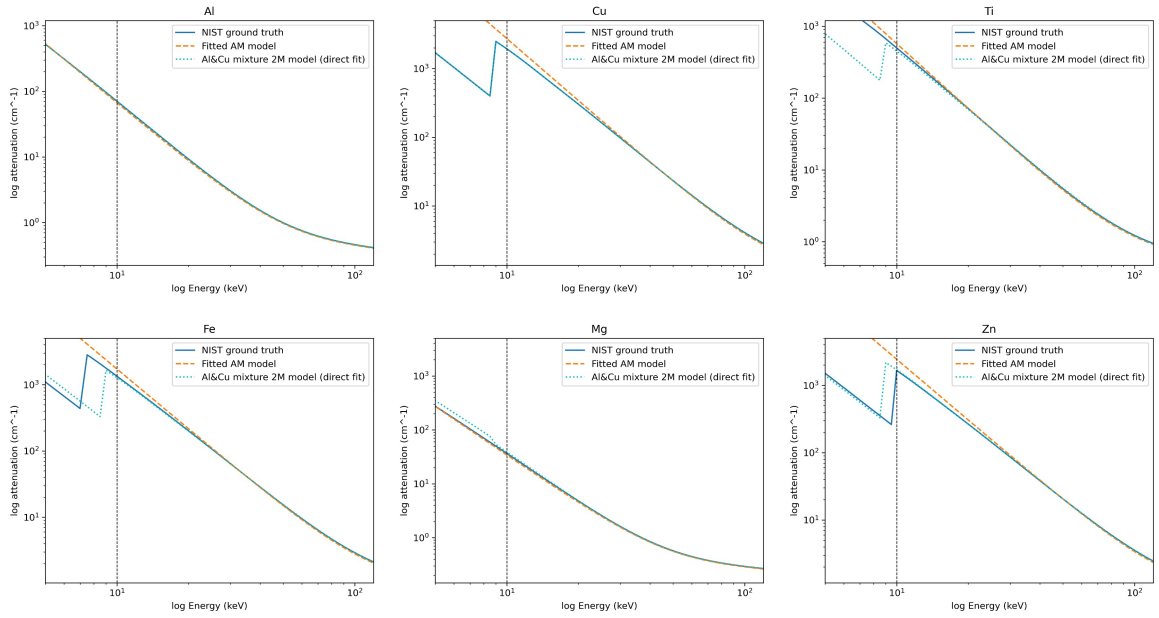

Figure 5.8: Attenuation fitted by the 2M and AM models, plotted alongside the NIST ground truth attenuation for Al, Cu, Ti, Fe, Mg, and Zn.

model provided comparable accuracy to the AM model. Regarding computational speed, as the 2M model required optimisations involving all linear combinations of attenuation of basis materials, it was approximately ten times slower than the AM model. This issue could potentially be addressed by pre-computing a table containing various combinations of attenuation values for the basis materials and then utilising this table to estimate the approximate positions of the measured values. This matter will be further discussed in detail in Chapter 6.

Figure 5.9 shows density and atomic number maps of the Ti & Fe phantom reconstructed using the 2M and AM models, respectively, with increasing noise levels resulting from a decrement in the initial intensity I_0 from 10^6 to 10^4, 10^3, and 500 ppx. Their corresponding quantitative results of the circular areas of interest are summarised in Table 5.4.

The reconstructed images became noisier as the value of I_0 decreased, as expected. However, the quantitative results for the densities and atomic numbers were not significantly affected. The results obtained using the 2M model showed a similar trend to that of the AM model (reconstructed density values slightly increased while atomic numbers

slightly decreased as the noise level increased), demonstrating comparable robustness in noise tolerance to the existing AM model.

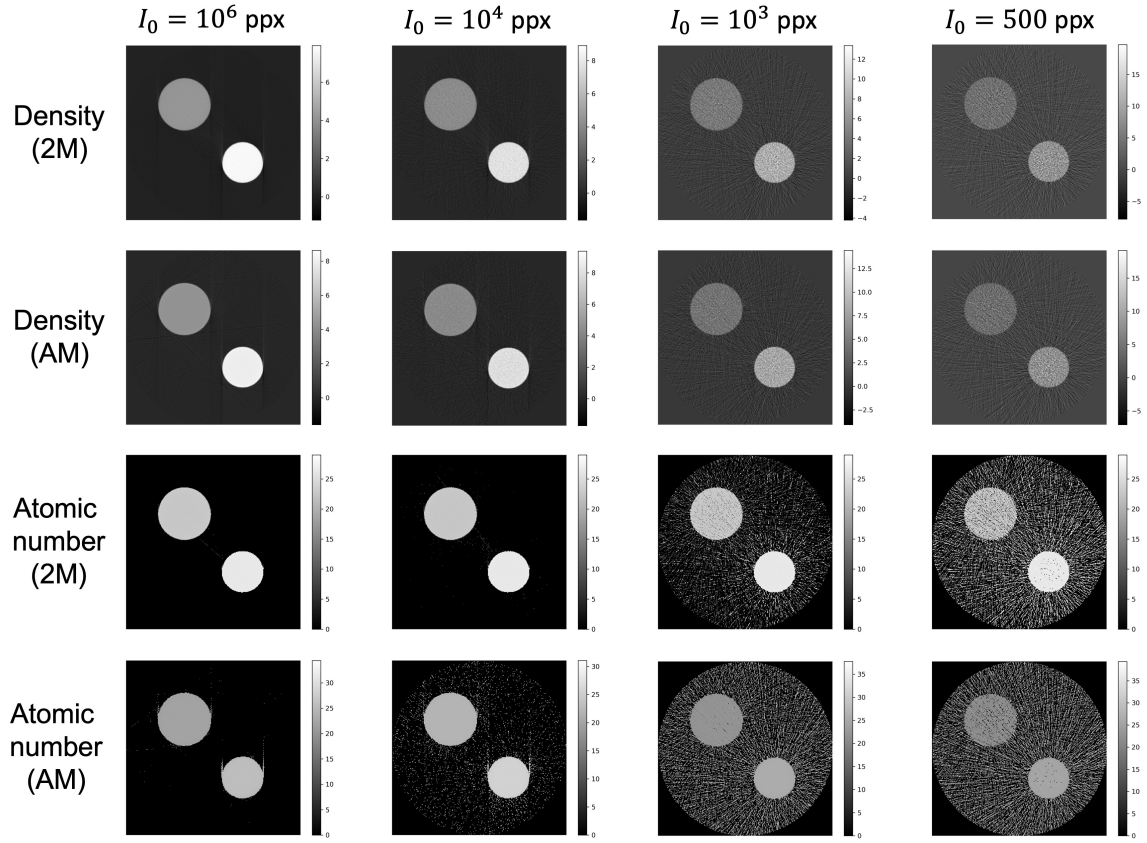

Figure 5.9: Density and atomic number maps of the Ti & Fe phantom (top circle - Ti; bottom circle - Fe), reconstructed using the 2M and AM models, respectively, with increasing noise levels resulting from a decrement in the initial intensity I_0 from 10^6 to 10^4, 10^3, and 500 ppx.

	$I_0 = 10^6$ ppx	$I_0 = 10^4$ ppx	$I_0 = 10^3$ ppx	$I_0 = 500$ ppx
ρ_{Ti} (gr/cm^3) (2M)	4.095	4.149	4.167	4.191
ρ_{Ti} (gr/cm^3) (AM)	4.237	4.217	4.225	4.267
ρ_{Fe} (gr/cm^3) (2M)	7.661	7.661	7.670	7.720
ρ_{Fe} (gr/cm^3) (AM)	7.765	7.756	7.751	7.824
Z_{Ti} (2M)	22.64	22.69	22.50	22.15
Z_{Ti} (AM)	21.81	21.97	21.77	21.27
Z_{Fe} (2M)	26.39	26.40	26.40	26.37
Z_{Fe} (AM)	25.42	25.45	25.42	25.41

Table 5.4: Density (ρ) and atomic number (Z) values for the Ti & Fe phantom with varying levels of added noise (where noise increases as the value of I_0 decreases), reconstructed by the 2M and AM models, respectively. These values are averaged over the region of interest within the circular area.

In summary, in this chapter, I found that:

1. In theory, the 2M model has the potential to achieve quantitative XCT and is overall more robust than the AM model, based on the analysis of tomographic reconstructions of some common materials.
    - It shows improved beam-hardening correction relative to the AM model (refer to Figure 5.5 and 5.7).
    - It provides quantitative results comparable to the AM model, with densities and atomic numbers registering a relative error within 10%.
2. One limitation of the 2M model is its inaccuracy for materials whose atomic numbers fall outside the range defined by the basis materials.
    - Selecting a higher atomic number material as one of the basis materials, such as Cu, can expand the applicability of the model to a broader range of materials within this range.
    - However, materials with higher atomic numbers display K-edge discontinuities at higher energies ($\geq$ 10 keV) which can affect the fitting process and impact the accuracy of quantitative results.
3. The optimisation process used in obtaining the 2M model, analogous to identifying the optimised solution in a table that lists varied combinations of attenuation values for the basis materials. This suggests that the 2M model has the potential to be simpler than the AM model in experiments, as it does not require spectrum information if this table can be obtained through direct measurements.

Therefore, I will explore the 2M model using real data in experiments to further investigate its ability in practice in the following chapters.

Chapter 6

Experimental Calibration of the Two-Material Model for Multi-Energy Imaging

In the previous chapter, I demonstrated through simulations that the 2M model serves as a robust attenuation model for obtaining quantitative information from materials and reducing beam-hardening artifacts in tomographically reconstructed images. In this chapter, I present the experimental calibration process that will enable us to implement this model through experiments.

As mentioned in Section 5.6.2, during experiments, I will measure a table of attenuation values (or equivalently, transmission values) for various combinations of pathlengths through the basis materials. I will use this table to estimate the approximate 2M decomposition of the measured multi-energy transmission values. I will first explain how I construct this table and, then explore various methods to extract the 2M model from this table.

6.1 Direct Measurement of Transmission Tables Using 2D Step Wedges

In this section, I illustrate how I measured the transmission tables using two step wedges. A step wedge is a calibration or test object made of a material with a stepped increase in thickness or density. These measurements would later be used to obtain the 2M model.

Since high-purity Aluminum (Al) is difficult to obtain in practice, I selected Silicon

(Si) with an atomic number of 14 and Copper (Cu) with an atomic number of 29 as the two basis materials. Matthew Shadwell constructed step wedges of increasing thickness for both materials (as depicted in Figure 6.1). Both wedges were created starting from layer 1 at the bottom, with equal thickness added in each step until reaching the top (layer 10). The thickness of each Si layer was 0.48 mm ± 0.01 mm, while that of each Cu layer was 0.08 mm ± 0.005 mm.

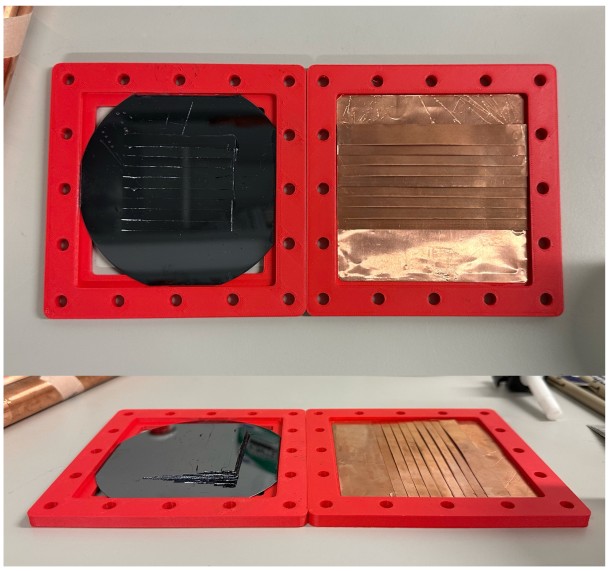

Figure 6.1: Step wedges of Si (left) and Cu (right). Both created starting from layer 1 at the bottom, with equal thickness added in each step until reaching the top (layer 10). Thickness of each layer: Si : 0.48 mm ± 0.01 mm; Cu : 0.08 mm ± 0.005 mm.

Benjamin Young, Adrian and I then imaged these step wedges using both low-energy and high-energy spectra. For low-energy imaging, we set the tube voltage to 60 kV and the tube current to 80 µA; for high-energy imaging, the tube voltage was set to 120 kV and the tube current to 60 µA. The exposure time was 0.25 seconds. The sketch of the experimental set-up is shown in Figure 6.2. The detector was positioned 835 mm from the X-ray tube, as far back as possible to minimise the detection of Compton scattered X-rays from the object (represented by green arrows). The sample was placed 200 mm from the tube, about 1/4 of the distance between the tube and the detector. This position was chosen as a trade-off to balance the effects of source scattered (off-focal) X-rays and Compton scattered X-rays. Assuming that the penumbral blurring from off-focal X-rays can be estimated as the product of the aperture diameter and the distance from the sample to the detector (635 mm), divided by the sample distance, the blurring in this

case was around 4.75 mm, as indicated by the orange ray paths in Figure 6.2. Therefore, placing the sample closer to the detector would reduce the blurring effect. However, assuming Compton scattering is equally distributed in all directions, placing the sample closer to the detector would result in a larger portion of scattered X-rays being detected. Additionally, we centred a 1.5 mm aperture through a lead plate in front of the X-ray tube window to minimise off-focal X-rays from the source. Without the aperture, the diameter of the off-focal X-ray source is 10 mm.

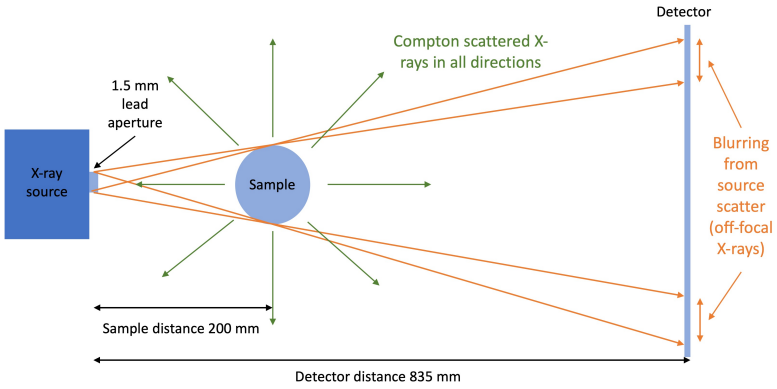

Figure 6.2: Sketch of the experimental set-up.

We took 1000 X-ray images (for the purpose of collecting sufficient data for mean and variance analysis) with the HeliScan MicroCT MkII from Thermo-Fisher Scientific for each of the following set of samples:

1. Darkfield (DF): Imaging was performed with the X-ray turned off.
2. Clearfield (CF) at 60 kV: Imaging without a step wedge, using a 0.5 mm Al filter.
3. Si Wedge at 60 kV: Imaging of a Si step wedge, using a 0.5 mm Al filter.
4. Cu Wedge at 60 kV: Imaging of a Cu step wedge, using a 0.5 mm Al filter.
5. Si & Cu Wedges at 60 kV: Imaging of Si and Cu step wedges placed on top of each other in a cross pattern, forming a 10 $\times$ 10 grid table, with a 0.5 mm Al filter.
6. Clearfield (CF) at 120 kV: Imaging without a step wedge, using a 0.5 mm Al filter and a 0.34 mm Cu filter.

7. Si Wedge at 120 kV: Imaging of a Si step wedge, using a 0.5 mm Al filter and a 0.34 mm Cu filter.

8. Cu Wedge at 120 kV: Imaging of a Cu step wedge, using a 0.5 mm Al filter and a 0.34 mm Cu filter.

9. Si & Cu Wedges at 120 kV: Imaging of Si and Cu step wedges, done in the same manner as for 60 kV, using a 0.5 mm Al filter and a 0.34 mm Cu filter.

The estimate transmission data T for each set of samples x is normalised as follows:

$$T = \frac{I}{I_0} = \frac{\text{mean}(x) - \text{mean}(DF)}{\text{mean}(CF) - \text{mean}(DF)}, \tag{6.1}$$

where I is the transmitted intensity, I_0 is the incident intensity, mean$(\cdot)$ represents the per-pixel average over those 1000 images, and CF is the clearfield data taken at either 60 kV or 120 kV, corresponding to the energy used for sample x.

Figure 6.3 shows the transmission images for sets 5 and 9, calculated using Equation 6.1, with the corresponding line profiles generated along the red lines marked in the images. In the images, from top to bottom, there is Si from layer 1 to layer 10, with thickness ranging from 0.48 mm to 4.8 mm. From left to right, there is Cu from layer 1 to layer 10, with thickness ranging from 0.08 mm to 0.8 mm. These two sets of data (sets 5 and 9) will be used to generate the two transmission tables for multi-energy imaging.

I extracted the average values within a smaller centered region inside each grid to minimise the effect of off-focal X-rays, and constructed the corresponding 10 $\times$ 10 transmission table, as shown in Figure 6.4. These images have values ranging from below 0.05 (very low transmission) to almost 0.9 (about 90% transmission). The top left corner indicates the transmission T after passing through one layer of Si and one layer of Cu, or equivalently, 0.48 mm of Si and 0.08 mm of Cu. Similarly, the grid location (3, 2) (third row, second column) represents the transmission after passing through three layers of Si and two layers of Cu, or equivalently, 3 $\times$ 0.48 mm of Si and 2 $\times$ 0.08 mm of Cu. Using these tables, one can obtain various combinations of transmission values, defined by different thicknesses of Si and Cu, at both low- and high-energy levels for multi-energy imaging. These combinations serve as look-up tables to estimate the mixture of Si and Cu

contained in the sample of interest. This then allows us to calculate the effective atomic number and density of that material (Equations 3.12 and 3.13 from Chapter 3). This approach is equivalent to the optimisation process I previously conducted in simulations (Section 5.4). The exact procedure will be illustrated in Section 7.1.

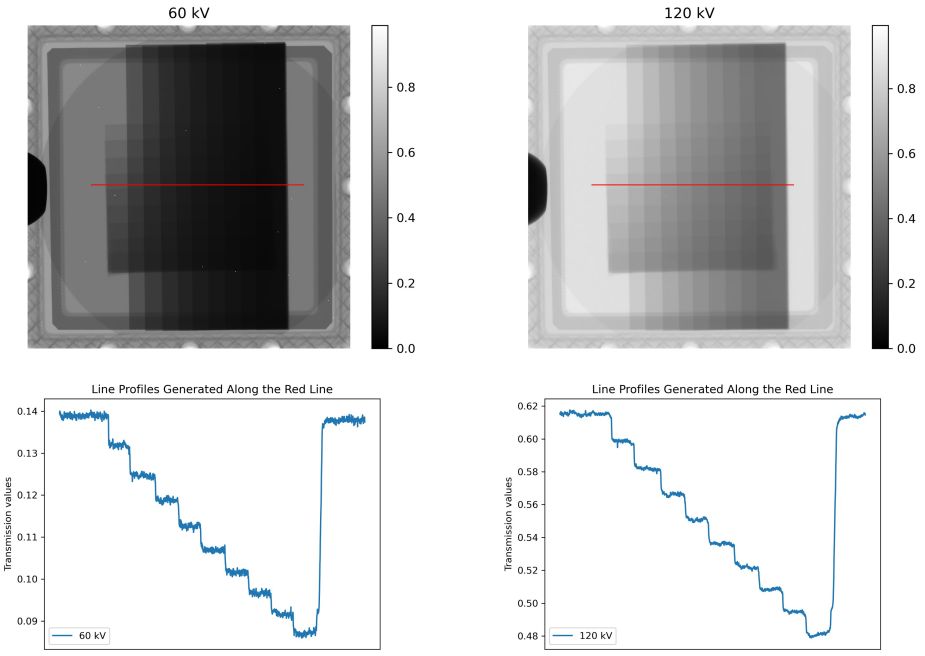

Figure 6.3: Transmission images for Si and Cu step wedges placed on top of each other in a cross pattern, forming a 10 × 10 grid of different material thickness, to provide calibration for the 2M model. The corresponding line profiles are generated along the red lines marked in the images. From top to bottom: Si from layer 1 to layer 10, with thickness ranging from 0.48 mm to 4.8 mm. From left to right: Cu from layer 1 to layer 10, with thickness ranging from 0.08 mm to 0.8 mm.

6.2 Analysis of Transmission Tables

In this section, I analyse the results of the two transmission tables obtained from the last section. Specifically, I generate the corresponding theoretical transmission table that would be expected, given the theoretical spectrum produced under the experimental settings, and compare them to those in Figure 6.4.

Figure 6.5 shows the two theoretical normalised spectra I would expect to be measured by the detector. These were calculated using the Python Spekpy library [42]. The low-

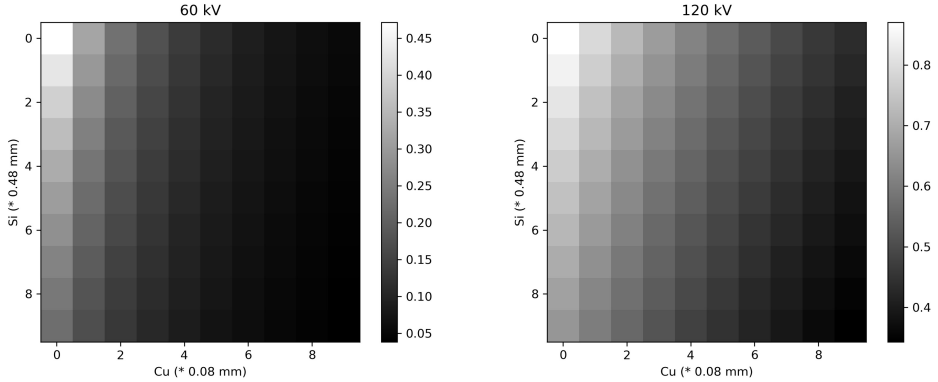

Figure 6.4: Transmission tables generated using Si and Cu step wedges at 60 kV and 120 kV, respectively. From top to bottom: Si from layer 1 to layer 10, with thickness ranging from 0.48 mm to 4.8 mm. From left to right: Cu from layer 1 to layer 10, with thickness ranging from 0.08 mm to 0.8 mm.

energy spectrum, $S_{d1}(E)$, was generated with a tube voltage of 60 kV and a 0.5 mm Al filter. The high-energy spectrum, $S_{d2}(E)$, was generated with a tube voltage of 120 kV, a 0.5 mm Al filter, and a 0.34 mm Cu filter. The detector had sensor protection that consisted of a carbon fibre with thickness of 2.5 mm, and an Al layer that was 0.25 mm thick. X-rays were detected by an amorphous Si layer behind a cesium iodide scintillator that was 0.7 mm thick. Both spectra were normalised so that their integrals (areas under the curve) equaled one.

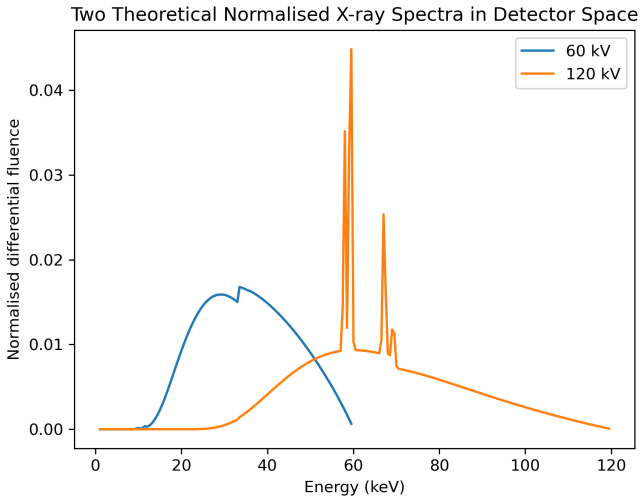

Figure 6.5: Two normalised spectra we would expect to be measured by the detector. The low-energy spectrum is generated at 60 kV with 0.5 mm Al filter (blue). The high-energy spectrum is generated at 120 kV with 0.5 mm Al filter and 0.34 mm Cu filter (orange).

The values in the theoretical transmission table were calculated as follows:

$$T_{theory} = \sum_{E} S_{di}(E) e^{-\mu_{Si} t_{Si} - \mu_{Cu} t_{Cu}}, \tag{6.2}$$

where $i = \{1, 2\}$, S_{di} corresponds to the two theoretical normalised spectra shown in Figure 6.5, μ_{Si} and μ_{Cu} represent the theoretical attenuation coefficients for Si and Cu, respectively, as retrieved from NIST.XCOM [28], t_{Si} and t_{Cu} denote the corresponding actual thicknesses of Si and Cu at that grid.

Figure 6.6 shows the two theoretical transmission tables calculated using Equation 6.2, and their absolute difference images with the corresponding experimental tables are presented in Figure 6.7. One can observe that the average difference at 60 kV was less than that at 120 kV. Nevertheless, both difference images exhibited some patterns (i.e., not random), indicating that the theoretical spectra used to calculate the table is probably not a good match to the actual spectra in the experiment. This discrepancy suggested that further work needs to be done in estimating the spectra, which will be discussed in Section 6.4.

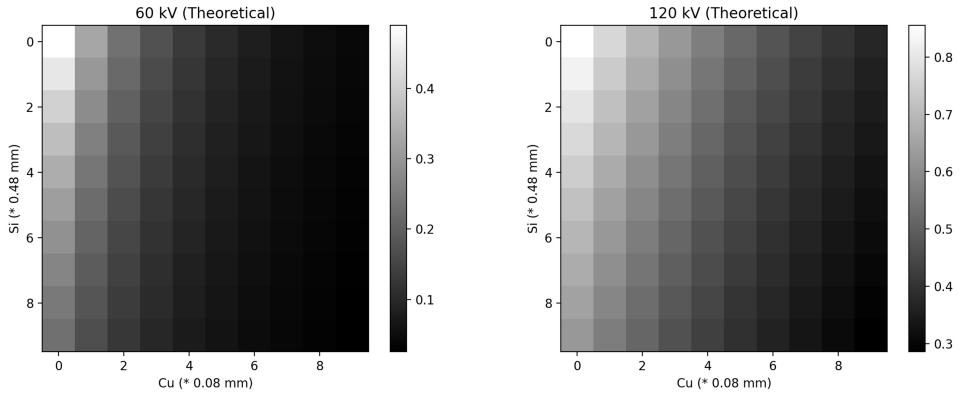

Figure 6.6: Theoretical transmission tables calculated for Si and Cu step wedges at 60 kV and 120 kV, respectively. From top to bottom: Si from layer 1 to layer 10, with thickness ranging from 0.48 mm to 4.8 mm. From left to right: Cu from layer 1 to layer 10, with thickness ranging from 0.08 mm to 0.8 mm.

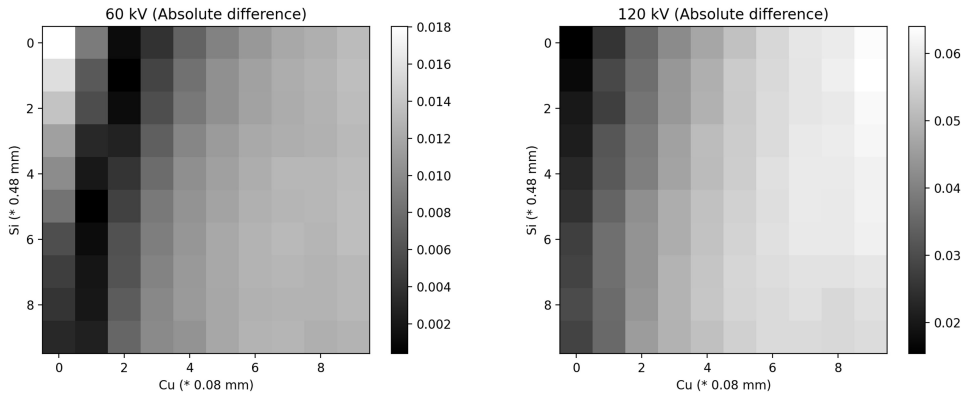

Figure 6.7: Absolute difference images between the experimentally obtained transmission tables and the theoretically calculated ones, at 60 kV and 120 kV. These differences suggest the modelled spectra may not be an accurate estimate of the actual spectrum.

6.3 Analysis of Relative Mean Energy of the Spectrum

Before delving into finding ways to match the theoretical spectrum with that detected in the experiment, I examined the relative mean energy of the spectrum after it passed through the single-material wedges (i.e., sets 3, 4, 7, and 8, as mentioned in Section 6.1). I compared values calculated from experiments to those generated theoretically to further demonstrate that the theoretically generated spectra were incorrect.

According to Section 4.2, I estimated the mean energy using variability in pixel values from repeat experiments as follows:

$$\gamma \langle E \rangle = \frac{\text{var}(x - \text{mean}(DF)) - \text{var}(DF)}{\text{mean}(x - \text{mean}(DF))}, \tag{6.3}$$

$$\gamma \langle E_0 \rangle = \frac{\text{var}(CF - \text{mean}(DF)) - \text{var}(DF)}{\text{mean}(CF - \text{mean}(DF))}, \tag{6.4}$$

where γ is a detector-dependent parameter, $\langle E \rangle$ is the mean energy after passing through the sample x, $\langle E_0 \rangle$ is the mean energy of the incident beam reaching the detector when there is no sample, var$(\cdot)$ represents the variance calculated over the corresponding 1000 images calculated using Python numpy.var library, mean$(\cdot)$ represents the average over those 1000 images, and CF is the clearfield data taken at either 60 kV or 120 kV.

I then computed the relative mean energy images, $\langle E \rangle / \langle E_0 \rangle$, by taking the ratio $\gamma \langle E \rangle / \gamma \langle E_0 \rangle$. Again, I extracted the average values within a smaller centered region inside each thickness step.

To calculate the theoretical mean energy passing through a certain thickness of the corresponding material (Si or Cu), I used the Python Spekpy library [42] to generate the spectrum, adding that amount of material as an extra filter. For example, when generating the mean energy of the spectrum after it passes through 0.48 mm of Si at 60 kV, I kept everything else unchanged but added an extra filter of that thickness of Si when generating $S_{d1}(E)$, and then computed the mean energy of that spectrum. Subsequently, I computed the theoretical relative mean energy by dividing this by the mean energy of the incident spectrum, namely $S_{d1}(E)$ or $S_{d2}(E)$, depending on the tube voltage used. The mean energy for $S_{d1}(E)$ was 32.03 keV, and for $S_{d2}(E)$ was 61.91 keV.

The results are illustrated in Figure 6.8. The error bar on the x-axis represents the uncertainty in the thickness of the step wedges, while the error bar on the y-axis represents the standard deviation of the values in the extracted regions divided by the square root of the number of points in that region. Notice that, as more materials were passed through, the relative mean energy increased progressively, except for the Cu wedge at 60 kV. This observation was a direct demonstration (or even measurement) of beam-hardening, which also emphasised the challenges of analysis in real XCT systems. The experimental data points were unstable, with the instability mainly arising from variance calculations. The experimental relative mean energy data deviated from the trend indicated by the theoretical calculations: both curves at 120 kV showed similar trends but with a different offset for the Si wedge, whereas both at 60 kV were lower than the theoretical values. This further demonstrated that the theoretical model did not account for all phenomena that happened experimentally.

6.4 Fitting the Spectrum to Obtain a 2M Model

If we assume all deviations from theory are due to an incorrect spectrum model, we can try to fit the correct spectrum to the experimental data. This approach would enable us to use optimisation methods to solve Equations 5.4 and 5.5 and perform tomography, as

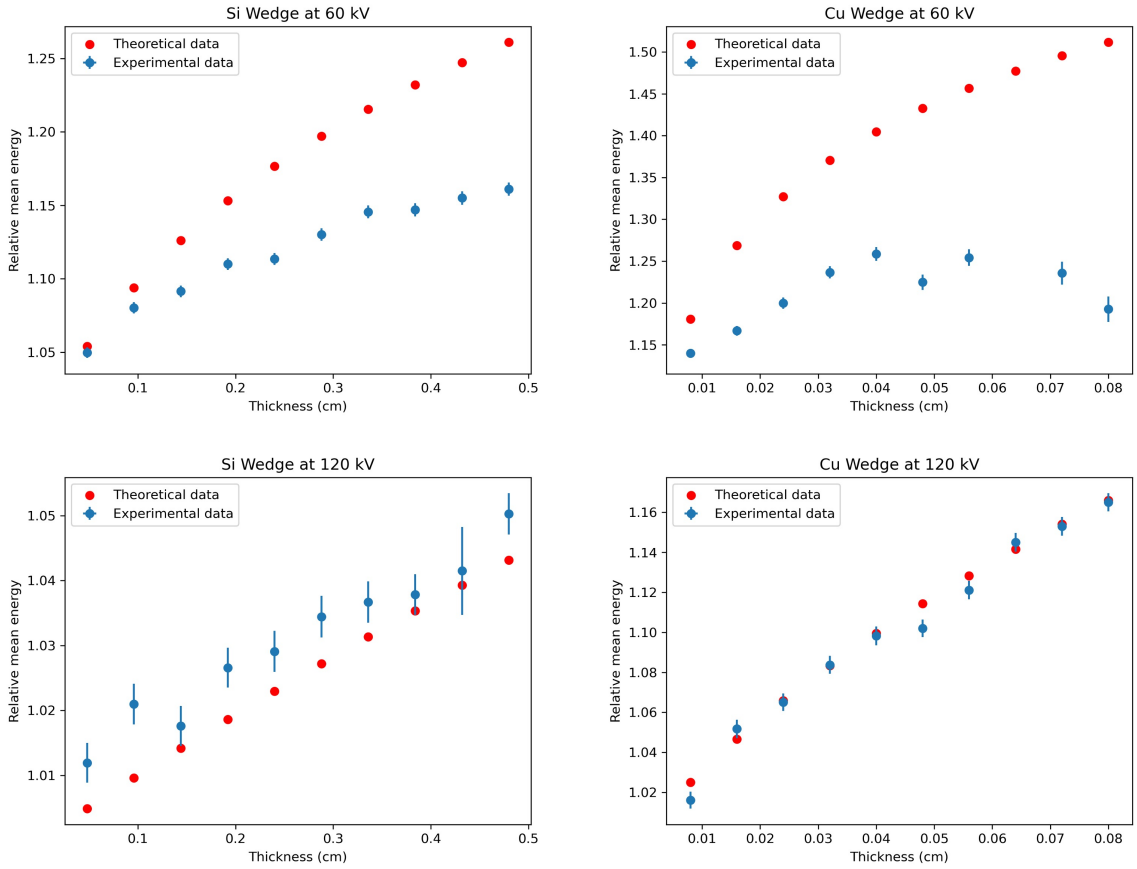

Figure 6.8: Relative mean energy analysis of the 1D Si and Cu step wedges, varying with material thickness, at 60 kV and 120 kV, respectively. Experimental data x-axis error bar: the uncertainty in the thickness of the step wedges; y-axis error bar: the standard deviation of the values in the extracted regions divided by the square root of the number of points in that region.

done in simulations (Section 5.4). In this section, I analyse the single-material wedges, namely sets 3, 4, 7, and 8, as mentioned in Section 6.1. This analysis elucidate why I did not choose to directly fit the two spectra using the obtained data, highlighting the challenges in this approach.

I plotted $-\ln(T)$ (where T is the transmission) as a function of the thickness of the corresponding material for the following three cases, as shown in Figure 6.9. Note that in the monochromatic case, $-\ln(T)$ is the attenuation and is directly proportional to thickness of material. Here I refer to $-\ln(T)$ as polychromatic attenuation for convention. The analysis process for these plots follows:

1. Experimental data

I calculated the transmission image for each set (3, 4, 7, and 8) using Equation 6.1. Similar to the process used in creating the transmission table for 2D data in Section 6.1, I extracted the average transmission values within a smaller centered region inside each thickness step. Taking $-\ln$ of these values yields the scattered points shown in Figure 6.9. The error bar on the x-axis represents the uncertainty in the thickness of the step wedges, while the error bar on the y-axis represents the standard deviation of the values in the extracted regions divided by the square root of the number of points in that region. In this case, they were so small that they were essentially within the circular points.

2. Theoretical data

   The theoretical transmission data T_{theory} were calculated as follows:

$$T_{theory} = \sum_{E} S_{di}(E) e^{-\mu_j t_j}, \tag{6.5}$$

   where $i = \{1, 2\}$, S_{di} corresponds to the two theoretical normalised spectra shown in Figure 6.5, j = Si or Cu, μ_j represents the theoretical attenuation coefficient for Si or Cu, as retrieved from NIST.XCOM [28], and t_j is the thickness given by the x-axis values.

3. Best fit data

   I directly fitted the spectrum in this case to obtain the best-fit data, $S_{f1}(E)$ and $S_{f2}(E)$, as shown in Figure 6.10. In both the 60 kV and 120 kV cases, I attempted to minimise the square error between the transmission table shown in Figure 6.4 and the table generated using the fitted spectra correspondingly.

   For 60 kV, the optimisation parameters were the thickness of the filters. The reason I varied only the thickness and material of filters when fitting the spectrum was that I observed that the data generated with the theoretical spectrum basically agreed with the trend of the experimental data (see Figure 6.9). Therefore, I assumed the spectrum at 60 kV accounted for most phenomena happening at the detector, and only minor adjustments needed to be made. I set three different filters to vary thickness: Al, Si, and Cu, and the initial guess was the theoretical spectrum $S_{d1}(E)$.

The best-fit spectrum, $S_{f1}(E)$, was given by Al of 0.5 mm and Cu of 0.0023 mm (no Si).

For 120 kV, I observed that the data generated with the theoretical spectrum was off the trend of the experimental data (see Figure 6.9). In this case, I started the initial guess with a normalised flat spectrum and allowed the spectrum parameters (heights of each bin) to vary directly to minimise the square error, which then gave the best-fit spectrum $S_{f2}(E)$ shown in Figure 6.10.

The transmission data generated by the best-fit spectra can be calculated using Equation 6.5, with $S_{di}(E)$ replaced by the best fit spectra $S_{fi}(E)$ accordingly.

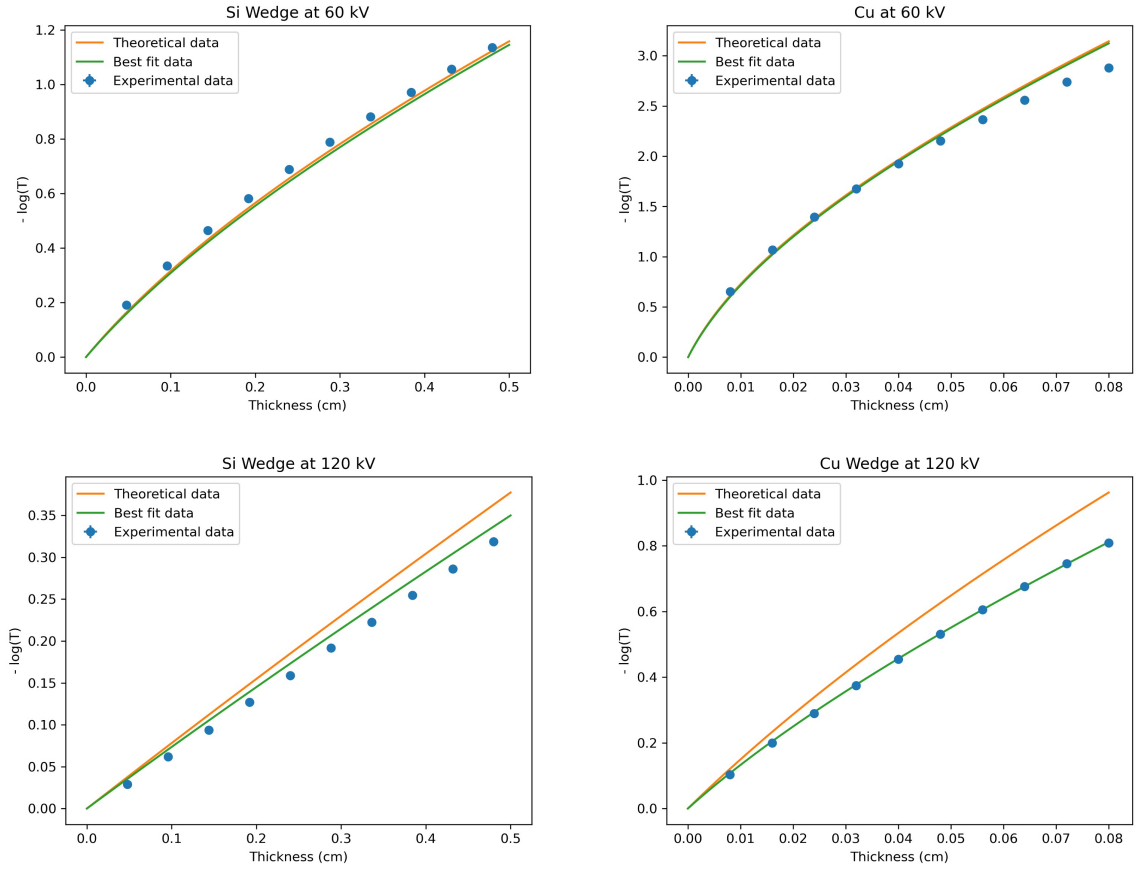

Figure 6.9: Polychromatic attenuation ($-\ln(T)$) analysis of the 1D Si and Cu step wedges, varying with material thickness, at 60 kV and 120 kV, respectively. Experimental data x-axis error bar: the uncertainty in the thickness of the step wedges; y-axis error bar: the standard deviation of the values in the extracted regions divided by the square root of the number of points in that region. Here, they are so small that they are essentially within the circular points.

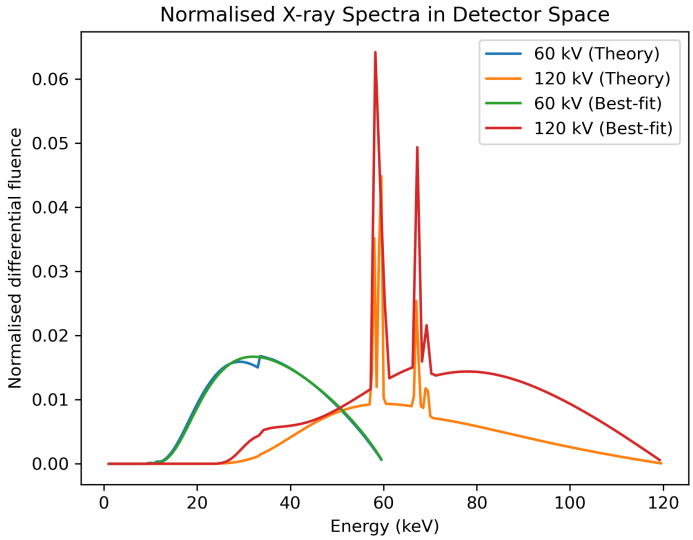

Figure 6.10: Two normalized best-fit spectra in the detector space, plotted alongside the two normalized theoretical spectra.

Even with the best-fit spectrum I obtained, the generated data still did not quite follow the trend of the experimental ones. Particularly in 60 kV Cu and 120 kV Si; I was not able to get the tail to match the correct trend (or shape). Additionally, in the difference images of the transmission tables obtained directly from experiments (Figure 6.4) and those generated using the best-fit spectra, I did not observe a random pattern, which would indicate a decent fit. This underscored the difficulties in directly fitting the spectrum and indicated that spectrum fitting alone might not account for all discrepancies. There could be other X-ray or matter interactions at play. The model did not account for everything that happened experimentally, and identifying the missing elements without more clues would be very challenging. This is also why the AM model has not been validated in experiments before — the difficulty in obtaining the exact spectra and accounting for all interaction phenomena, both of which are necessary for the AM model.

One interesting observation was that, while the theoretical polychromatic attenuation aligned more closely with the experimental data at 60 kV than at 120 kV, the opposite held for the relative mean energy analysis, especially for Cu at 60 kV. This discrepancy certainly highlighted the insufficiency of the model and suggested that this could be a valuable focus for future work.

6.5 Other Methods to Obtain a 2M Model

Since spectrum fitting proved to be not useful, I investigated other methods that could be applied using the transmission tables to obtain the 2M model.

Upon inspecting the experimental polychromatic attenuation data illustrated in Figure 6.9, I observed that the smooth variations may be captured by a polynomial function. I fitted a 2nd-order polynomial, $P_1(t_{Si}, t_{Cu})$ and $P_2(t_{Si}, t_{Cu})$, where t_{Si} and t_{Cu} represent the thicknesses of Si and Cu, to the transmission table at 60 kV and 120 kV, respectively.

Given the measured transmission values at two energies for an object of interest, m_1 and m_2, I calculated the object's equivalent thickness as a combination of t_{Si} and t_{Cu}, as:

$$t_{Si},\ t_{Cu} = \underset{t_{Si}, t_{Cu}}{\operatorname{argmin}} \left[\left(P_1(t_{Si}, t_{Cu}) - m_1 \right)^2 + \left(P_2(t_{Si}, t_{Cu}) - m_2 \right)^2 \right], \tag{6.6}$$

where the optimisation method used for finding t_{Si} and t_{Cu} was the Nelder-Mead algorithm [47] provided by the Python scipy.optimize.minimize library. However, through simple simulations, I found that this approach did not extrapolate well beyond the measured regions of the table and became very unstable.

Another approach is that one can use the table directly as a model. By employing linear extrapolation, we can extend the table to data outside its original range, for example, from 10 × 10 to 20 × 20, or even to accommodate negative thicknesses. This extension allows us to handle a wider range of measurement data for objects of interest. Subsequently, we can use linear interpolation to calculate equivalent thickness as a combination of t_{Si} and t_{Cu}. This approach will be discussed in the next chapter.

In summary, I have presented the 2D transmission tables along with their analysis and have demonstrated why spectrum fitting was not chosen using the experimental calibration process: the model did not account for everything that happened experimentally. Therefore, I investigated other methods that could be applied, using the transmission tables directly, to obtain the 2M model. Theoretically, these methods should be less time-consuming as they do not require a massive fitting procedure to find the optimised results through random combinations and are also easier to implement as they do not require spectrum information. These will be further discussed and applied in the next chapter to examine the performance of the 2M model in experiments.

Chapter 7

Implementation of the Two-Material Model Through Experiments

In this chapter, I explain in detail how I use the transmission table directly as a model to obtain a 2M model and test its performance on several test objects. This represents original work on implementing the two-material model experimentally with polychromatic data using a conventional X-ray detector. The results highlight the complexities introduced when dealing with real data compared with the scatter-free models used in simulation.

7.1 Developing the 2M Model Directly from Measurements

In Figure 6.4, the directly measured transmission tables contain only 10 thickness steps for each basis material. These are generally insufficient for accurately estimating measurements across a wide range of objects. Therefore, in this section, I first describe how I expanded these tables to accommodate measurement data beyond the directly measured regions, as well as discuss how I enhanced the resolution to address finer thickness steps in the basis materials. Subsequently, I illustrate how I used the extended and refined tables to obtain a 2M model for determining the equivalent thickness of the object of interest.

7.1.1 Extending, Linearly Extrapolating, and Cubic-Spline Interpolating the Transmission Tables

In this section, I present how I extended, extrapolated and smoothed the directly measured transmission tables in Figure 6.4 to handle a wider range of measurement data of interest.

Extending: I first extended the tables presented in Figure 6.4 from 10 × 10 to 11 × 11 by adding the first row (layers of Cu with 0 layers of Si) and the first column (layers of Si with 0 layers of Cu), using the data from the 1D step wedges (sets 3, 4, 7, 8 mentioned in Section 6.1). By definition, the transmission for 0 layers of Si and 0 layers of Cu (top-left corner) is simply 1. The extended tables are shown in Figure 7.1.

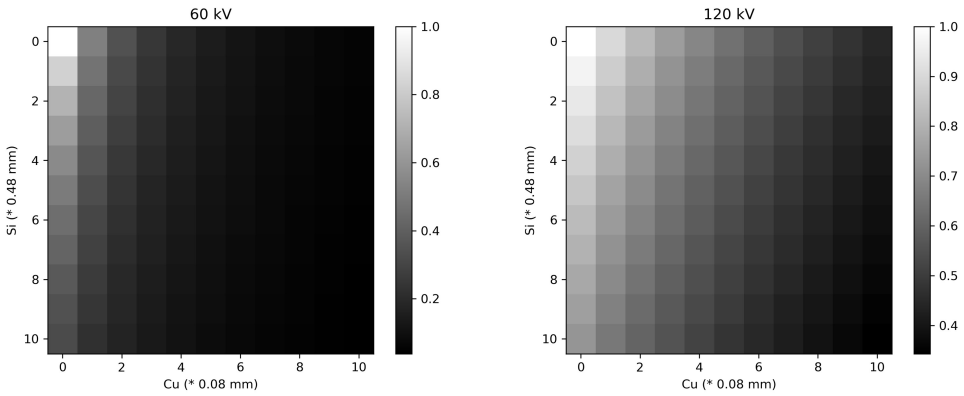

Figure 7.1: Extended transmission tables generated at 60 kV and 120 kV, respectively. From top to bottom: Si with thickness ranging from 0.0 mm to 4.8 mm. From left to right: Cu with thickness ranging from 0.0 mm to 0.8 mm.

Linear Extrapolating: To enable the transmission table to account for a wider range of measurement data, I applied linear extrapolation to extend the table from its original maximum thickness of x and y to $3x$ and $3y$ maximum thickness, in this case from 11 × 11 to 33 × 33. Observing that the values in the transmission table vary slowly and that the change in gradient due to beam-hardening is much lower when passing through substantial amounts of Si and Cu (reaching the edges) than when going through little material. I assumed that for each row and column, the gradient thereafter follows that provided by the last point and the second-to-last point of that row or column. The extrapolated tables are shown in Figure 7.2.

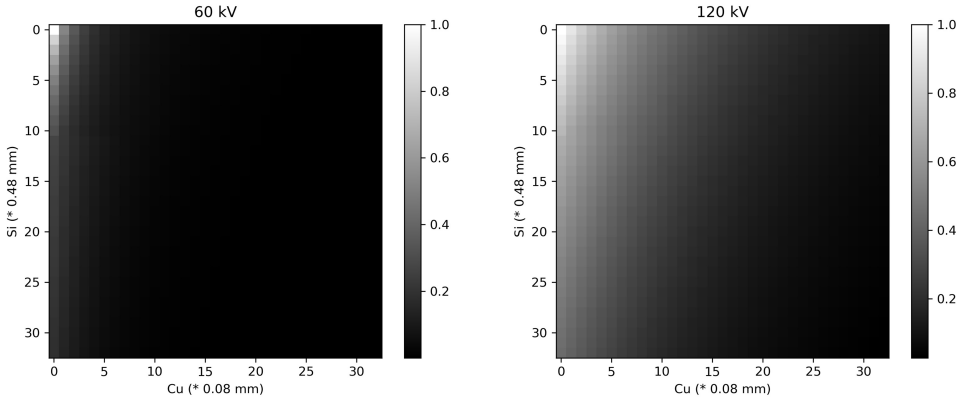

Figure 7.2: Extrapolated transmission tables generated at 60 kV and 120 kV, respectively. From top to bottom: Si with increasing thickness, starting from 0.0 mm and increasing at an interval of 0.48 mm. From left to right: Cu with increasing thickness, starting from 0.0 mm and increasing at an interval of 0.08 mm.

Cubic-Spline Interpolating: Finally, I created a smoother table using code from Andrew that was realised based on the scipy.interpolate.RectBivariateSpline library in Python. I zoomed in on the table by a factor of 10, transforming it from 33 × 33 to 330 × 330. Note that in this step, I did not extrapolate any new data; I simply increased the table's resolution. Consequently, Si now increases at an interval of 0.048 mm, and Cu at an interval of 0.008 mm. The smoothed tables are illustrated in Figure 7.3. These tables will also be the ones I use for subsequent analysis. For convention, I refer to them as Tab_1 for 60 kV and Tab_2 for 120 kV.

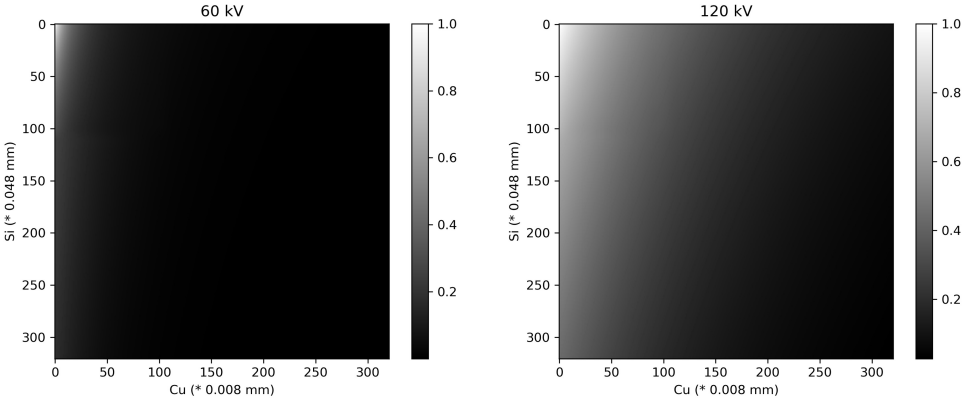

Figure 7.3: Smoothed extrapolated transmission tables generated at 60 kV and 120 kV, respectively. From top to bottom: Si with increasing thickness, starting from 0.0 mm and increasing at an interval of 0.048 mm. From left to right: Cu with increasing thickness, starting from 0.0 mm and increasing at an interval of 0.008 mm.

7.1.2 Linear Interpolation to Obtain a 2M Model

In this section, I explain how I used the extrapolated and smoothed tables from Figure 7.3 to determine the equivalent thickness of the object of interest. I further employ a simulated example to examine the performance of this method in comparison to the method applied to the simulations (Section 5.4).

For the transmission data obtained for an object, T_1 at 60 kV, and T_2 at 120 kV, I determined the equivalent thickness as a combination of Si thickness of B_1 cm and Cu thickness of B_2 cm using Tab_1 and Tab_2 through the following steps:

1. I first identified the position (x_0, y_0) on the table that minimise the square error:

$$x_0,\ y_0 = \underset{x,y}{\operatorname{argmin}} \left[\left(Tab_1(x,y) - T_1\right)^2 + \left(Tab_2(x,y) - T_2\right)^2 \right]. \tag{7.1}$$

   Note that this is only robust because T_1 and T_2 are both monotonic functions of B_1 and B_2.

2. I extracted a 3×3 region from each table with (x_0, y_0) as the center.

3. I fitted a linear surface $a_i x + b_i y + c_i$ (where $i = \{1, 2\}$, a_i, b_i and c_i are constants) to the 3×3 region of Tab_1 and Tab_2, respectively.

4. Lastly, within the 3×3 region, I pinpointed the position (x_{min}, y_{min}) by finding:

$$x_{min},\ y_{min} = \underset{x,y}{\operatorname{argmin}} \left[\left(a_1 x + b_1 y + c_1 - T_1\right)^2 + \left(a_2 x + b_2 y + c_2 - T_2\right)^2 \right]. \tag{7.2}$$

The determined position (x_{min}, y_{min}) essentially provides the thicknesses B_1 and B_2: $B_1 = 0.0048 \cdot y_{min}$ cm, and $B_2 = 0.0008 \cdot x_{min}$ cm.

To validate the proposed approach of using the transmission table directly, I compared the B_1 and B_2 values obtained by the proposed interpolation method with those estimated using the optimisation method from Chapter 5, given ideal spectra. Figure 7.4 shows the solved B_1 and B_2 of a simulated example of 10 increasing thicknesses of marble ($CaCO_3$), from 0.2 mm to 2mm. Marble has an effective atomic number of 15.35, so it falls within the atomic number range determined by the basis materials. I plotted the solved Si thickness B_1 and Cu thickness B_2 at each thickness using:

1. Solutions obtained through the method applied in simulations (Section 5.4), i.e., direct optimisation using the Python scipy.optimize.minimize library and the theoretical spectra presented in Figure 6.5.

2. Solutions obtained using the interpolation method on the 10 × 10 theoretical tables generated with the theoretical spectra (Figure 6.6).

3. Solutions derived from the interpolation method on the extrapolated and smoothed 330 × 330 theoretical tables. These tables utilised the same extrapolation and smoothing method presented in the preceding section but applied to these theoretical 10 × 10 tables.

For consistency, I relied on all simulated results, i.e., theoretical tables generated using theoretical spectra produced by the Python Spekpy library, rather than the experimental tables previously presented. The results presented in Figure 7.4 provided insight into how the extrapolation and zoom-in resolution approaches can improve the accuracy of determining B_1 and B_2, using the method described in Section 5.4 as a ground truth (since this method has proven effective). The thicknesses derived from the 10 × 10 tables were unstable and did not follow the trend set by the ground truth, and the B_2 values were all confined to nearly 0 since the ground truth values of Cu thickness were below the thickness steps of the tables (< 0.008 cm). In contrast, those obtained from the 330 × 330 tables aligned more closely with the ground truth values. The instability in the B_2 values derived from the 330 × 330 table might also be due to the small ground truth values of Cu. This could be tested and confirmed by using a material other than marble, which contains a higher portion of Cu. However, this was omitted here due to time constraints. Furthermore, the results validated that this interpolation method applied to the 330 × 330 tables would yield reasonable outcomes. Therefore, we can proceed to test the performance of the method on experimental samples, which will be detailed in the next section.

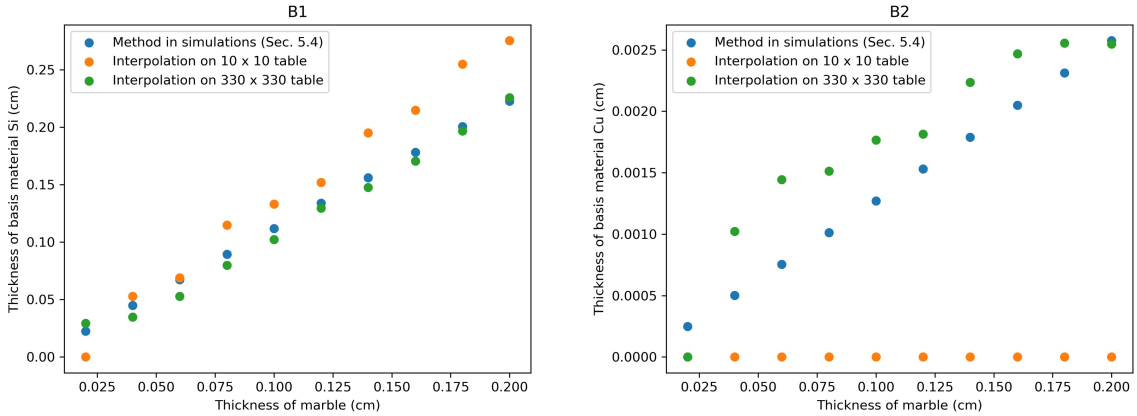

Figure 7.4: Si thickness B_1 and Cu thickness B_2 determined for a simulated example of 10 increasing thicknesses of marble ($CaCO_3$) using: (1) the method from simulations (Section 5.4); (2) interpolation method on the 10 $\times$ 10 theoretical tables; (3) interpolation method on the 330 $\times$ 330 theoretical tables. The B_2 values derived from the 10 $\times$ 10 table are all confined to nearly 0 since the ground truth values of Cu thickness are below the thickness steps of the tables ($<$ 0.008 cm).

7.2 Experimental Testing of the 2M Model on Test Objects

7.2.1 Method

In this section, I apply the method presented in Section 7.1.2 to different test objects to examine the performance of the 2M model.

I used the following sets of test objects (also called phantoms), as illustrated in Figure 7.5:

1. **Al step wedge:** 13 steps, each with a thickness of 0.4 mm, placed on 1 mm of glass.

2. **Steel step wedge:** 10 steps, each with a thickness of 0.1 mm, placed on 1 mm of glass. The cut-off edge of the thickest step is marked by a black line.

3. **Glass step wedge:** 6 steps, each with a thickness of 1 mm. The cut-off edge of the thickest step is marked by a black line.

4. **Ti step wedge:** 10 steps, each with a thickness of 0.1 mm. The thickest step is placed on a smaller region to the right of the second-thickest step (See Figure 7.5).

5. **Three cylinders:** An Al cylinder with a diameter of 8.25 mm, a marble cylinder with a diameter of 10.4 mm, and a steel cylinder with a diameter of 2.5 mm (from Hozan Ball Point Wrench Set W-110, made of alloy steel).

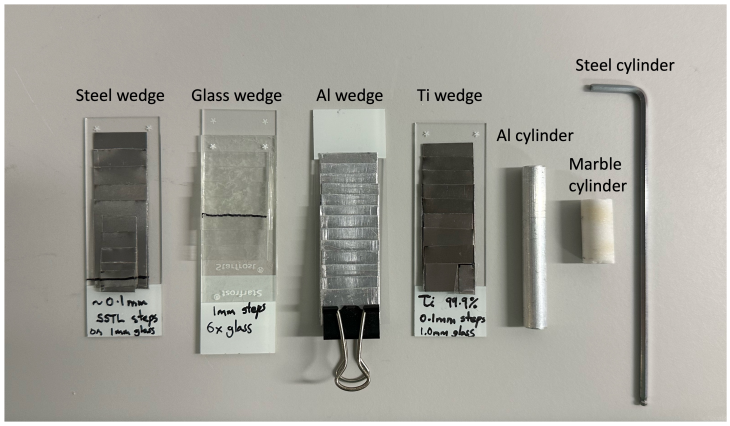

Figure 7.5: Phantoms used to test the performance of the 2M model. From left to right: steel wedge (10 steps), glass wedge (6 steps), Al wedge (13 steps), Ti wedge (10 steps), Al cylinder ($d = 8.25$ mm), marble cylinder ($d = 10.4$ mm), and steel cylinder ($d = 2.5$ mm).

Andrew and I took X-ray images (or radiographs) of each set using the same experimental setup described in Section 6.1, at both 60 kV and 120 kV. For set 5, we bound the three cylinders together and took images of them as a single unit. For each set, we averaged 40 captured X-ray images to improve the signal-to-noise ratio.

I calculated the transmission image for each set at 60 kV and 120 kV using Equation 6.1. Figure 7.6 displays the transmission image calculated at 60 kV for the five sets of phantoms.

Using the method described in Section 7.1.2, I determined the equivalent thicknesses B_1 and B_2 of the basis materials Si and Cu. For sets 1 - 4, I extracted the average values from a smaller centered region within each thickness step and calculated B_1 and B_2 for each step. For set 5, I performed this calculation for every pixel.

For each set, I plotted:

1. Experimentally reconstructed B_1 and B_2 and compared them to the ideally reconstructed B_1 and B_2 values. These ideal values were calculated first by generating

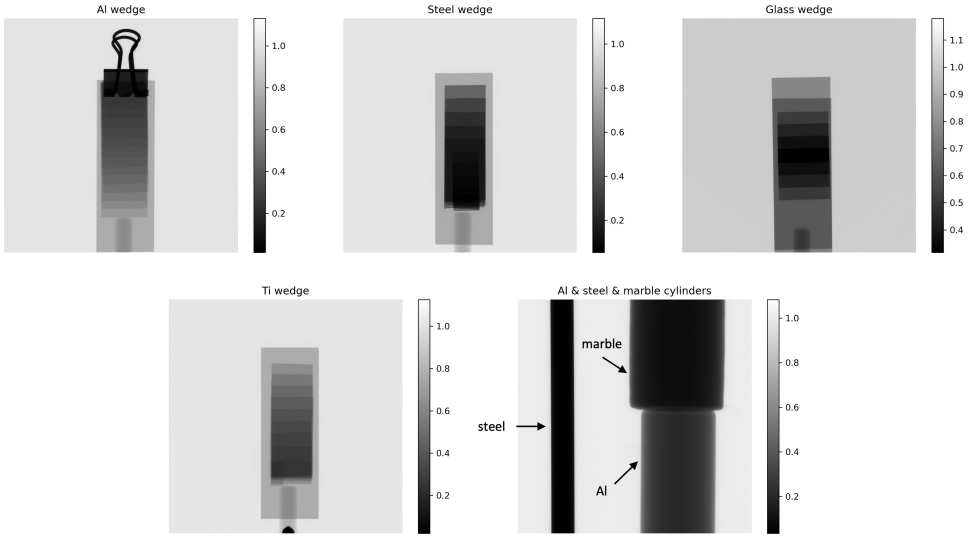

Figure 7.6: Transmission images calculated at 60 kV for Al, steel, glass, and Ti step wedges, as well as the three-cylinder phantom (from left to right: the thinnest rod is steel; top right is marble; bottom right is Al).

the corresponding ideal transmission values for given material thicknesses. Then, I applied the same procedure in simulation with the optimisation method provided by the Python scipy.optimize.minimize library, assuming the spectra to be S_{d1} and S_{d2} as outlined in Section 6.2. Note that it was previously observed that the spectra S_{d1} and S_{d2} did not correctly predict attenuation and therefore were unlikely to be accurate. Consequently, these values were not theoretical but merely provide an indication of the general trend that B_1 and B_2 should approximately follow.

2. I also plotted reconstructed effective mass thickness, denoted as ϱ (density multiplied by thickness), which was calculated for each pixel in the radiographs by:

$$\varrho = B_1\rho_{Si} + B_2\rho_{Cu}, \tag{7.3}$$

where ρ_{Si} and ρ_{Cu} are densities of Si and Cu, respectively, retrieved from NIST.XCOM [28]. Note that since radiographs are projections of densities, it is not possible to directly reconstruct the density of a step wedge or cylinder without a priori knowledge about the objects (such as their projected thickness).

Since the material thickness and density are known, for these samples we can com-

pare with theoretical values given by:

$$\varrho_{theory} = \sum_i t_i \rho_i, \tag{7.4}$$

where t_i corresponds to the thickness (in cm) of material i with density ρ_i. For example, ϱ_{theory} for the first step of the Al wedge (0.4 mm thick Al on a 1 mm glass slide) should be $0.04\rho_{Al} + 0.1\rho_{glass}$.

7.2.2 Results & Discussions

Note that in this section, 'reconstructed B_1 and B_2' refer to the thickness of Si (B_1) and Cu (B_2) calculated pixelwise in each particular radiograph using the method described in Section 7.1.2. The term 'reconstructed effective mass thickness' refers to the corresponding value determined using Equation 7.3.

Figures 7.7 and 7.8 show the reconstructed equivalent Si thickness B_1, and equivalent Cu thickness B_2, and the reconstructed effective mass thickness, for the glass, Al, Ti, and steel step wedges (sets 1 - 4). The reconstructed effective mass thicknesses are plotted alongside theoretical curves generated using Equation 7.4, with straight lines fitted to the reconstructed data, and the reconstructed B_1 and B_2 values are plotted together with their corresponding ideal reconstruction data. Note that they are ordered in increasing density as well as atomic number: glass ($\rho_{eff} = 2.23$ gr/cm^3, $Z_{eff} = 11.65$), Al ($\rho = 2.7$ gr/cm^3, $Z = 13$), Ti ($\rho = 4.506$ gr/cm^3, $Z = 22$), and steel ($\rho = 7.86$ gr/cm^3, $Z = 26$).

From the B_2 image of glass and Al wedges (in Figure 7.7), one can observe that the ideal values were negative, which was as expected because glass and Al fall outside the atomic number range defined by the basis materials, as discussed in Chapter 5 where negative values were required. However, since I did not find a robust way for the transmission tables to cover this range, so most of the time, they were confined to 0. This caused the algorithm to compensate with less Si, resulting in inaccuracies. Nevertheless, the gradients in the reconstructed effective mass thickness for glass and Al wedges roughly followed the trend of the theoretical predictions.

I attempted to extrapolate the table to account for negative values using linear extrapolation. Essentially, each point in the negative part was derived from calculations

involving three points from the original (positive) table. However, this negative extrapolation produced extremely unstable results during the analysis, so I chose not to use this approach. For future work, it might be beneficial to find an extrapolation method that takes the entire table into account, rather than just three points, to generate a smoother negative section, which could potentially lead to more stable results.

When inspecting the Ti and steel wedges, both of which fall within the range defined by the basis materials, it was surprising that their gradients in the reconstructed effective mass thickness significantly deviated from the trend of the theoretical ones. From their B_1 and B_2 images, it was evident that the reconstructed B_1 was higher than the ideal one, while B_2 was lower than the ideal one, indicating that one or both measurements of the basis material wedges contained significant unknowns about either the spectra or other X-ray interactions not modelled.

Figure 7.9 displays the reconstructed B_1 and B_2 maps for the three-cylinder phantom (set 5), with line profiles generated along the red, green, and blue lines, respectively. These profiles are plotted alongside the values that would ideally be obtained. Figure 7.10 depicts the reconstructed effective mass thickness map for the three-cylinder phantom. Line profiles generated along the red, green, and blue lines are also shown, compared with the theoretical values derived from Equation 7.4.

The B_1 and effective mass thickness images for marble (ρ_{eff} = 2.7 gr/cm^3, Z_{eff} = 15.35) and Al generally agreed with the ideal and theoretical predictions. However, there were artifacts at the edges of the Al cylinder reconstructions: double cylinders (additional edge-like features) in the reconstructed images and sudden turning points in the line profiles. These artifacts were potentially result from the solution crossing over the original regions of the tables into extrapolated regions (around 5 mm thick matching the thickest Si step). On the other hand, the reconstructed parts for steel significantly deviated from the predictions. Specifically, it underestimated the amount of Cu (B_2) and compensated with a larger amount of Si (B_1), which was incorrect but consistent with the B_1 and B_2 results for the steel step wedge shown in Figure 7.7. The flat tops in the B_1 images for steel indicated that the solved Si thickness reached the boundaries or edges of the transmission table.

From the results of the radiograph analysis, it appeared that errors increased as the

atomic number or density increased. In most cases, due to the inaccurate underestimation of Cu, the algorithm attempted to compensate with more Si, resulting in significant errors.

Upon examining the B_1 and B_2 maps of the three-cylinder phantom, I concluded that it was highly likely that there were substantial uncertainties or phenomena not captured in the model for the measurements of the Cu step wedge. One potential explanation for these results could be Compton scattering recaptured at the detector. Assuming that Compton scattered X-rays travel in all directions, I can estimate the fraction of the total scattered X-rays that would be detected by dividing the area of the detector by the area of a sphere with a radius equal to the distance from the object to the detector. This fraction was around 3.5%, which should be insignificant. However, generally, higher density is associated with greater Compton scattering, and since Cu has density of 8.96 gr/cm^3, it is particularly susceptible. During the measurement of the Cu wedge, scattered X-rays may have been measured, causing our original table to record more transmission data than expected. Consequently, this could lead to predictions of much less Cu than theoretically expected.

Another potential factor affecting the measurements could be off-focal X-rays from the source. Despite our efforts to center a 1.5 mm lead aperture to mitigate this issue, there may still be some leakage that could blur the images. From Figure 6.2, this could cause blurring in the images by merging data from neighboring steps of the step wedge.

In summary, in this chapter, I have illustrated the method of applying the transmission tables to measured data to obtain a 2M model and tested its performance with several phantoms composed of different materials. The resulting errors between the reconstructed experimental data and theoretical predictions showed greater deviations with increasing atomic number or density of the target material being imaged. The overall significant discrepancy indicated that the model requires improvement for proper implementation in experiments. I have also outlined potential reasons that can be considered as future directions.

While I had the tools to perform tomographic reconstruction from radiographs taken from different viewing angles, this would not be successful (i.e., free of artifacts) until the discrepancies between the expected and measured projections are reduced.

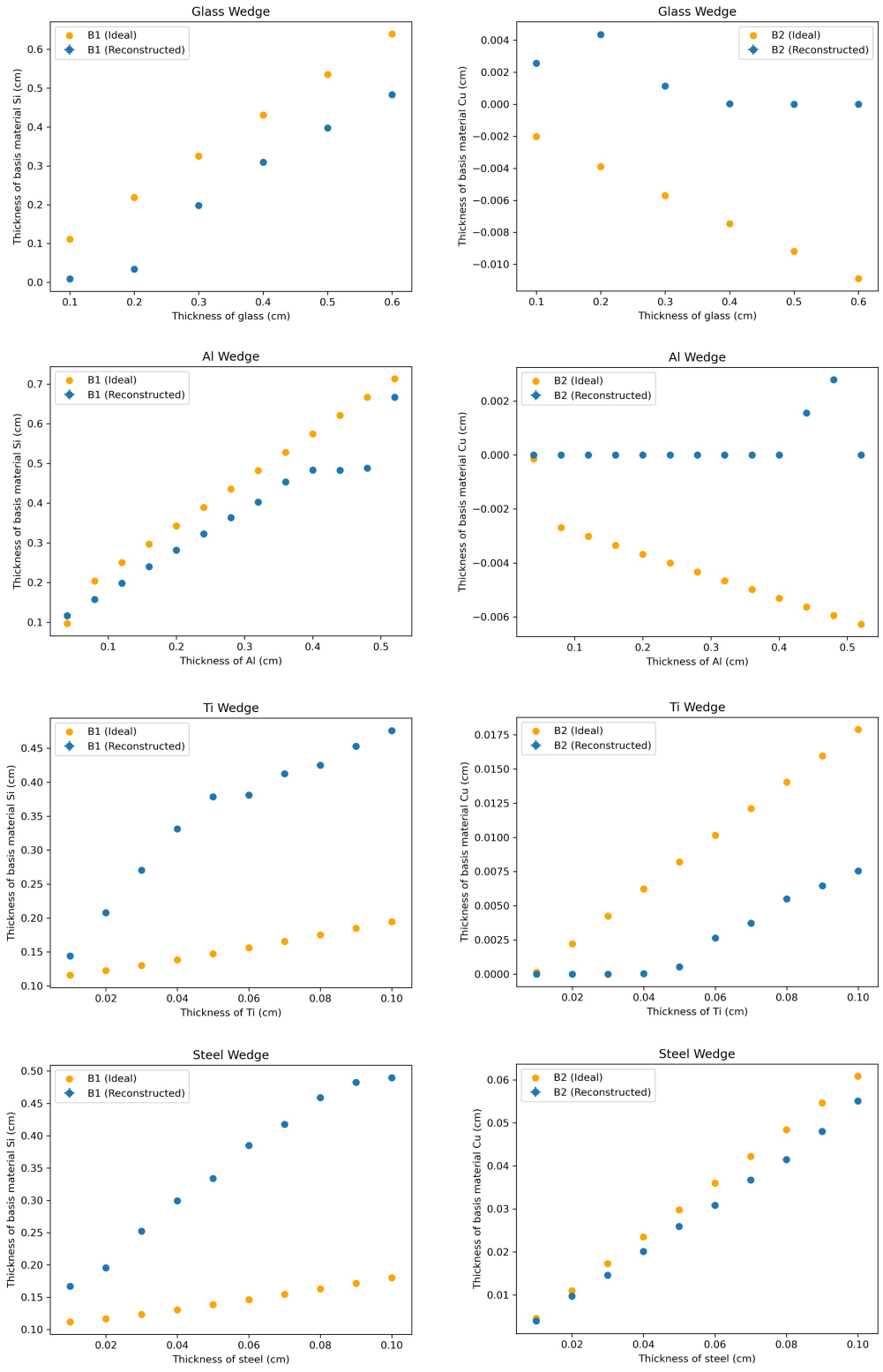

Figure 7.7: Reconstructed equivalent Si thickness B_1 and equivalent Cu thickness B_2 for the glass, Al, Ti, and steel step wedges, plotted alongside values from ideal reconstructions. Reconstructed data x-axis error bar: the uncertainty in the thickness of the step wedges; y-axis error bar: the standard deviation of the values calculated in the extracted regions divided by the square root of the number of points in that region. Here, they are so small that they are essentially within the circular points.

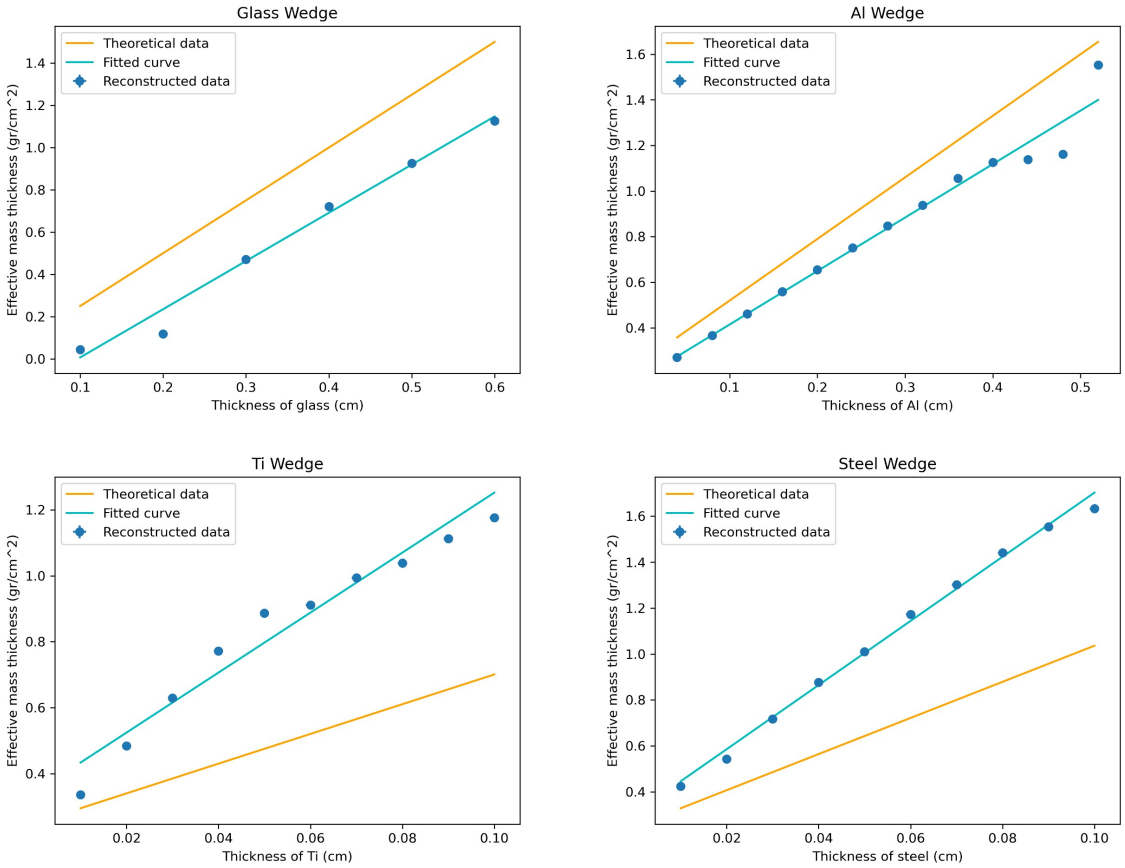

Figure 7.8: Reconstructed effective mass thicknesses for the glass, Al, Ti, and steel step wedges, with a linear curve fitted (cyan), and plotted alongside theoretical curves. Reconstructed data x-axis error bar: the uncertainty in the thickness of the step wedges; y-axis error bar: the standard deviation of the values calculated in the extracted regions divided by the square root of the number of points in that region. Here, they are so small that they are essentially within the circular points.

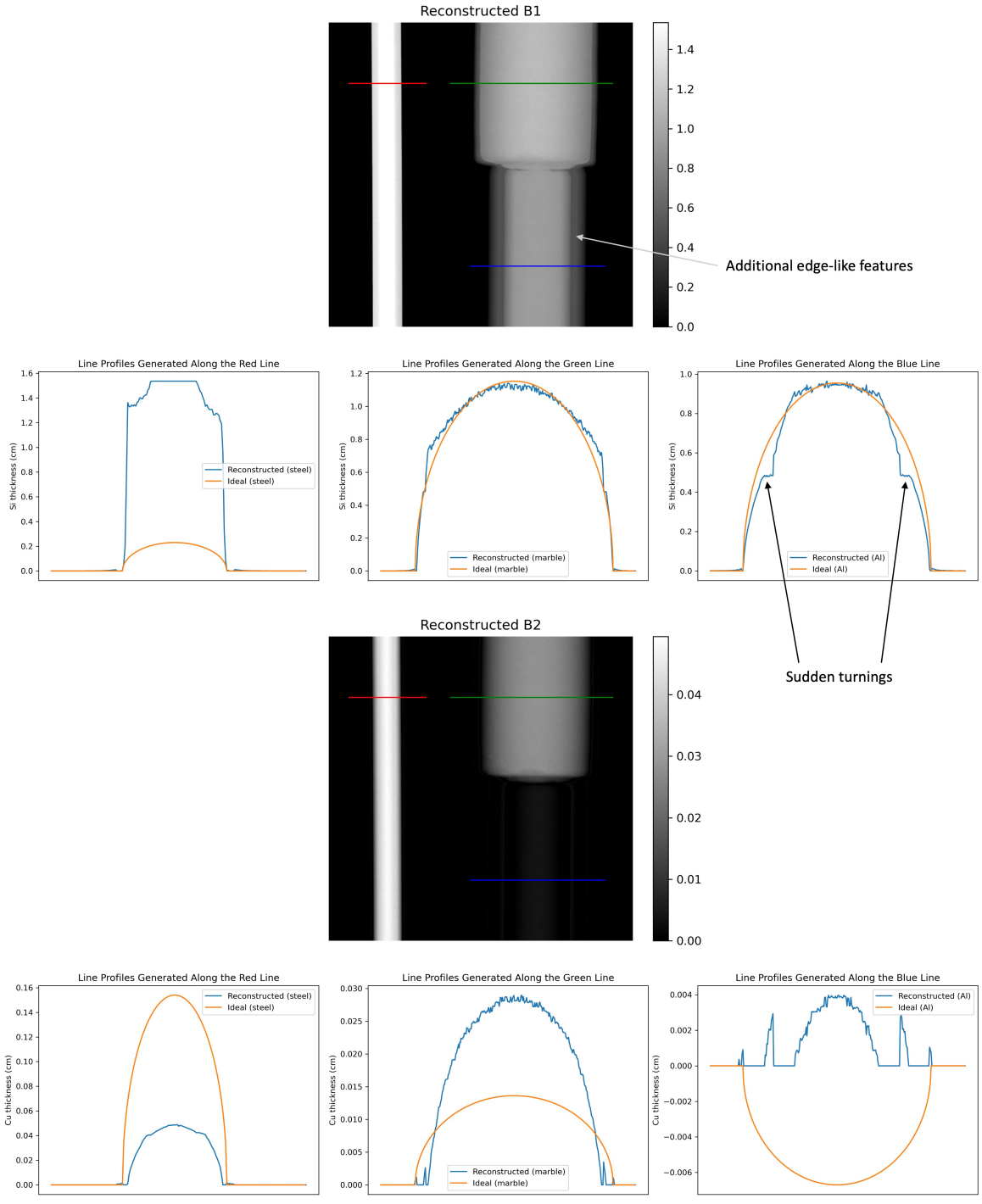

Figure 7.9: Reconstructed equivalent Si thickness B_1 and Cu thickness B_2 maps for the three-cylinder phantom. The leftmost, thinnest rod is steel; the top right is marble; the bottom right is Al. The corresponding line profiles are generated along the red lines (for steel), green lines (for marble) and blue lines (for Al).

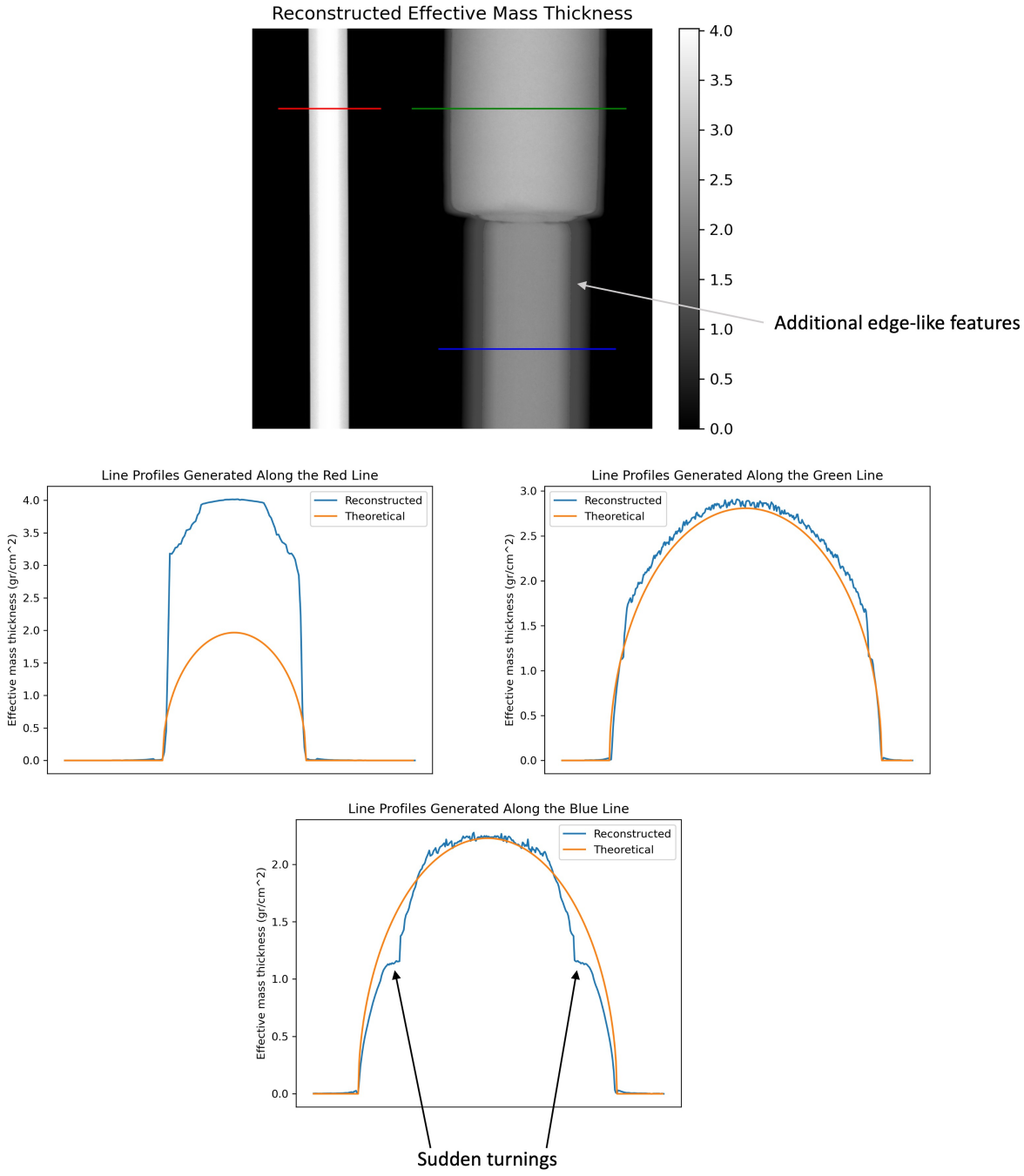

Figure 7.10: Reconstructed effective mass thickness map for the three-cylinder phantom. The leftmost, thinnest rod is steel; the top right is marble; the bottom right is Al. The corresponding line profiles are generated along the red line (for steel), green line (for marble) and blue line (for Al).

Chapter 8

Conclusions & Future Work

8.1 Concluding Remarks

In this work, we proposed a two-material (2M) model, inspired by [33], to obtain quantitative measurements in multi-energy XCT and mitigate beam-hardening artifacts. This model has the potential to be simpler than the well-known Alvarez-Macovski (AM) model as it does not require knowledge of the spectrum. The AM model approximates the X-ray attenuation for a material as a simple function of its density, atomic number, and the energy of X-rays. The 2M model assumes that X-ray attenuation for a material can be represented as a linear combination of the attenuation of two known materials (i.e., basis materials). Given the ratio of these materials the density and atomic number of the target material can be estimated. This work is, to my knowledge, the first time that the 2M model has been applied to polychromatic radiation in a standard laboratory configuration.

Through simulations, I demonstrated that the 2M model is more robust in the presence of some uncertainties than the AM model. It showed improved beam-hardening correction and provided comparable quantitative results (with densities and atomic numbers having a relative error within 10%) compared to the AM model for phantoms composed of different materials. It was observed that for materials with atomic numbers outside the range defined by the two basis materials, negative volume fractions of the basis materials were required. However, modeling such negative fractions in the lab practice can be challenging. Therefore, one consideration when applying the 2M model is the choice of basis materials. A limitation of the 2M model is its inaccuracy for materials whose atomic numbers fall outside the range defined by the basis materials. Opting for a higher atomic number material as one of the basis materials, such as Cu with an atomic

number of 29 in this work, expands the applicability of the model to a broader range of materials. However, higher atomic number materials exhibit K-edge discontinuities in their attenuation curves at higher energies ($\geq$ 10 keV), which can affect the fitting process and impact the accuracy of quantitative results. Note that based on simulation results, the choice of Cu as one of the basis materials was acceptable for the 2M model.

Through experiments, I showed that the exact form of the spectra was hard to obtain by direct fitting, since our theoretical model for generating the expected spectra does not yet accurately account for all phenomena occuring in the experiment. The exact form of the spectra is required for the AM model; however, it is not necessary for the 2M model. As an alternative, I used a transmission table containing various combinations of transmission (equivalently attenuation) values for the basis materials, constructed by imaging two step wedges, Si and Cu. I then used this table directly to estimate the approximate positions of the measured values. Theoretically, this method should be less time-consuming as it does not require a massive fitting procedure to find the optimised results through random combinations and is also more accurate and easier to implement as it does not require spectrum information or a model at all. I applied the 2M model obtained using this method to several phantoms composed of different materials to test its performance. However, the results showed larger errors than expected. The resulting errors between the reconstructed experimental data and theoretical predictions showed greater deviations with increasing atomic number or density of the target material being imaged, particularly larger for Ti and steel. One potential factor for this is Compton scattering, which is more significant for higher density, causing scattered X-rays to be measured during the measurement of the Cu wedge, so the table possibly recorded more transmission data than expected. Another potential factor is that the off-focal X-rays from the source were not completely blocked, which could cause blurring in the images by merging data from neighboring steps of the step wedge. The trend of the reconstructed experimental data for low-atomic number materials (glass, Al, and marble) followed the theoretical predictions; the errors mainly came from the table not accounting for negative values.

In summary, the experimental work uncovered some important discrepancies between model predictions and measured transmission; understanding these discrepancies will be

essential for achieving quantitative XCT.

8.2 Future Directions

Future work should focus on investigating the 2M model in laboratory XCT, in the following directions:

1. Investigating the cause for the discrepancy in X-ray transmission through high-atomic number materials. This can be done by properly modeling the X-ray source using multicolor particle simulation software, such as TOPAS [48], to see if the Compton scattered X-rays and off-focal X-rays play an important role in each case.

2. Extrapolating the transmission table to account for negative values to further decrease the error for materials that fall outside the range defined by the basis materials. As mentioned in Section 7.2.2, the current negative extrapolation model is very unstable. Due to time constraints, I used the one with only positive values. However, it is worth considering finding an extrapolation method that takes the entire positive table into account to generate a smoother negative section. This should lead to more stable results for some material combinations.

3. Further investigating spectrum fitting. Although this method was time-consuming, it showed promising results in simulations. It is worth trying other fitting methods, as well as considering missing parts in the detector space (this can also be investigated through modeling the X-ray sources mentioned in step 1 of future directions) to obtain the exact form of the spectrum and run optimisations to find solutions directly.

4. Using other basis materials. In this work, Cu was chosen as one of the basis materials in both simulations and experiments. However, it was observed that its high atomic number can significantly affect the reconstruction of target materials. It is reasonable to try a relatively low-atomic number material, such as Ti, to redo the experiments (as well as simulations) to see how the results will change.

5. Improving experimental setups. For example, a better aperture (smaller diameter) for the source to minimise the off-focal X-rays, and an anti-scatter grid for the detector to minimise the effects of scattering. Additionally, step-wedges with less uncertainty in thickness or higher purity may be developed.

6. Tomographic reconstructions. Due to time constraints, I concluded the experiment part by discussing only radiography reconstructions (the simulations were all on tomography reconstructions). Although Andrew and I took the data for tomography reconstructions of the three-cylinder phantom, because of the large inaccuracy in the steel cylinder as seen in the radiographs, the tomographic reconstructed slice of this phantom exhibited significant artifacts. Therefore, if through the previous steps it is possible to obtain decent results for radiography, the next step will be to test on tomography.

Overall, the 2M model showed some potential in achieving quantitative XCT. However, this work demonstrates that significant further work needs to be done to understand the complete X-ray interactions involved before this model can be implemented successfully in the lab.

This work emphasises that if we can eliminate all scattering that distorts the accuracy of measurements in experiments and develop the model to account for negative transmission (or attenuation) values, the 2M model can (1) effectively eliminate beam-hardening artifacts in tomographic reconstructions and (2) provide quantitative results, such as the density and atomic number of materials being imaged, as proven through simulations.

Bibliography

[1] Jiang Hsieh, Brian Nett, Zhou Yu, Ken Sauer, Jean-Baptiste Thibault, and Charles A Bouman. "Recent advances in CT image reconstruction". *Current Radiology Reports* 1 (2013), pp. 39–51.

[2] Elliot K. Fishman. *MSD Manual Professional Edition*. 2017.

[3] K Wells and DA Bradley. "A review of X-ray explosives detection techniques for checked baggage". *Applied Radiation and Isotopes* 70.8 (2012), pp. 1729–1746.

[4] Xiaochuan Pan, Jeffrey Siewerdsen, Patrick J La Riviere, and Willi A Kalender. "Anniversary Paper: Development of x-ray computed tomography: The role of Medical Physics and AAPM from the 1970s to present". *Medical physics* 35.8 (2008), pp. 3728–3739.

[5] Martine Wevers, Greet Kerckhofs, Gregory Pyka, Els Herremans, Annelies Van Ende, Roel Hendrickx, and E Wilderjans. "X-ray computed tomography for non-destructive testing". In: *International Conference on Industrial Computed Tomography*. 2012.

[6] Alexander Gall, Bernhard Fröhler, Julia Maurer, Johann Kastner, and Christoph Heinzl. "Cross-virtuality analysis of rich X-ray computed tomography data for materials science applications". *Nondestructive Testing and Evaluation* 37.5 (2022), pp. 566–581.

[7] MA Jardine, JA Miller, and Megan Becker. "Coupled X-ray computed tomography and grey level co-occurrence matrices as a method for quantification of mineralogy and texture in 3D". *Computers & Geosciences* 111 (2018), pp. 105–117.

[8] Jörg Stelzner and Sebastian Million. "X-ray computed tomography for the anatomical and dendrochronological analysis of archaeological wood". *Journal of Archaeological Science* 55 (2015), pp. 188–196.

[9] Tim K Lowenstein and Bärbel Hönisch. “The use of Mg/Ca as a seawater temperature proxy”. *The Paleontological Society Papers* 18 (2012), pp. 85–100.

[10] Maleeha Mashiatulla, Ryan D Ross, and D Rick Sumner. “Validation of cortical bone mineral density distribution using micro-computed tomography”. *Bone* 99 (2017), pp. 53–61.

[11] Rodney A Brooks and Giovanni Di Chiro. “Beam hardening in x-ray reconstructive tomography”. *Physics in medicine & biology* 21.3 (1976), p. 390.

[12] DL Sawkey and BA Faddegon. “Determination of electron energy, spectral width, and beam divergence at the exit window for clinical megavoltage x-ray beams”. *Medical physics* 36.3 (2009), pp. 698–707.

[13] M Paziresh, AM Kingston, SJ Latham, WK Fullagar, and GM Myers. “Tomography of atomic number and density of materials using dual-energy imaging and the Alvarez and Macovski attenuation model”. *Journal of Applied Physics* 119.21 (2016).

[14] Andreas Maier, Stefan Steidl, Vincent Christlein, and Joachim Hornegger. “Medical imaging systems: An introductory guide” (2018).

[15] Klara Steklova, Andrew Fielding, Levi Beeching, Adrian P Sheppard, and Andrew M Kingston. “A study of off-focal radiation in transmission geometry x-ray sources”. *In Proc. 12th Conference on Industrial Computed Tomography, iCT 2023* (2023).

[16] Masahiro Endo, Takanori Tsunoo, Nobuyuki Nakamori, and Katsuya Yoshida. “Effect of scattered radiation on image noise in cone beam CT”. *Medical physics* 28.4 (2001), pp. 469–474.

[17] GH Glover. “Compton scatter effects in CT reconstructions”. *Medical physics* 9.6 (1982), pp. 860–867.

[18] J Rinkel, L Gerfault, F Esteve, and JM Dinten. “A new method for x-ray scatter correction: first assessment on a cone-beam CT experimental setup”. *Physics in Medicine & Biology* 52.15 (2007), p. 4633.

[19] William D McDavid, Robert G Waggener, William H Payne, and Michael J Dennis. "Correction for spectral artifacts in cross-sectional reconstruction from x rays". *Medical physics* 4.1 (1977), pp. 54–57.

[20] Graham Davis, Nitin Jain, and James Elliott. "A modelling approach to beam hardening correction". In: *Developments in X-ray Tomography VI*. Vol. 7078. SPIE. 2008, pp. 423–432.

[21] Robert E Alvarez and Albert Macovski. "Energy-selective reconstructions in x-ray computerised tomography". *Physics in Medicine & Biology* 21.5 (1976), p. 733.

[22] CK Egan, SDM Jacques, MD Wilson, MC Veale, P Seller, AM Beale, RAD Pattrick, PJ Withers, et al. "3D chemical imaging in the laboratory by hyperspectral X-ray computed tomography". *Scientific reports* 5.1 (2015), p. 15979.

[23] Raju Kumar, Mariana Mar Lucas, Charalampos Lampadaris, Lillian Austin, and Bilal Kosar. "Characterization of X-ray anode and absorption edges". *Group* 1 (2018), p. 1.

[24] Jiang Hsieh. "Computed tomography: principles, design, artifacts, and recent advances" (2003).

[25] Edward L Nickoloff and Howard L Berman. "Factors affecting x-ray spectra." *Radiographics* 13.6 (1993), pp. 1337–1348.

[26] Mansour Ashoor, Afrouz Asgari, Abdollah Khorshidi, and Ali Rezaei. "Evaluation of Compton attenuation and photoelectric absorption coefficients by convolution of scattering and primary functions and counts ratio on energy spectra". *Indian Journal of Nuclear Medicine: IJNM: the Official Journal of the Society of Nuclear Medicine, India* 30.3 (2015), p. 239.

[27] Edward Uhler Condon and Halis Odabasi. *Atomic structure*. CUP Archive, 1980.

[28] MJ Berger, JH Hubbell, SM Seltzer, J Chang, JS Coursey, R Sukumar, DS Zucker, and K Olsen. "XCOM: Photon cross sections database, 2010". *DOI* 10 (2010), T48G6X.

[29] Ferdi Akman, Rıdvan Durak, Mehmet Fatih Turhan, and Mustafa Recep Kaçal. "Studies on effective atomic numbers, electron densities from mass attenuation coefficients near the K edge in some samarium compounds". *Applied Radiation and Isotopes* 101 (2015), pp. 107–113.

[30] G Christ. "Exact treatment of the dual-energy method in CT using polyenergetic X-ray spectra". *Physics in Medicine & Biology* 29.12 (1984), p. 1501.

[31] *Radiology | SUNY Upstate*. Accessed: 20 Oct, 2023.

[32] Qiheng Yang, WK Fullagar, GR Myers, SJ Latham, T Varslot, AP Sheppard, and AM Kingston. "X-ray attenuation models to account for beam hardening in computed tomography". *Applied Optics* 59.29 (2020), pp. 9126–9136.

[33] Thorsten Sellerer, Sebastian Ehn, Korbinian Mechlem, Manuela Duda, Michael Epple, Peter B Noël, and Franz Pfeiffer. "Quantitative dual-energy micro-CT with a photon-counting detector for material science and non-destructive testing". *PLoS One* 14.7 (2019), e0219659.

[34] RC Murty. "Effective atomic numbers of heterogeneous materials". *Nature* 207.4995 (1965), pp. 398–399.

[35] Kyongtae T Bae and Bruce R Whiting. "CT data storage reduction by means of compressing projection data instead of images: feasibility study". *Radiology* 219.3 (2001), pp. 850–855.

[36] Johan Nuyts, Bruno De Man, Jeffrey A Fessler, Wojciech Zbijewski, and Freek J Beekman. "Modelling the physics in the iterative reconstruction for transmission computed tomography". *Physics in Medicine & Biology* 58.12 (2013), R63.

[37] JH Siewerdsen, LE Antonuk, Y El-Mohri, J Yorkston, W Huang, JM Boudry, and IA Cunningham. "Empirical and theoretical investigation of the noise performance of indirect detection, active matrix flat-panel imagers (AMFPIs) for diagnostic radiology". *Medical physics* 24.1 (1997), pp. 71–89.

[38] RJ Schoelkopf, AA Kozhevnikov, DE Prober, and MJ Rooks. "Observation of "photon-assisted" shot noise in a phase-coherent conductor". *Physical review letters* 80.11 (1998), p. 2437.

[39] Glenn F Knoll. *Radiation detection and measurement*. John Wiley & Sons, 2010.

[40] Andrew M Kingston, Wilfred K Fullagar, Glenn R Myers, and Adrian P Sheppard. "Imaging Mean Energy of X-ray Spectra through Intensity Variation in Radiographs with an Example Application to Beam Hardening Correction." *Microscopy and Microanalysis* 24.S2 (2018), pp. 110–111.

[41] Qiheng Yang, Wilfred Fullagar, Mahsa Paziresh, Glenn Myers, Shane Latham, Adrian Sheppard, and Andrew Kingston. "Spectral information from photon statistics in x-ray radiography and computed tomography". *Physical Review A* 106.1 (2022), p. 013511.

[42] Gavin Poludniowski, Artur Omar, Robert Bujila, and Pedro Andreo. "SpekPy v2. 0—a software toolkit for modeling x-ray tube spectra". *Medical Physics* 48.7 (2021), pp. 3630–3637.

[43] Jerrold T Bushberg and John M Boone. *The essential physics of medical imaging*. Lippincott Williams & Wilkins, 2011.

[44] Jorge Nocedal and Stephen J Wright. *Numerical optimization*. Springer, 1999.

[45] Ciyou Zhu, Richard H Byrd, Peihuang Lu, and Jorge Nocedal. "Algorithm 778: L-BFGS-B: Fortran subroutines for large-scale bound-constrained optimization". *ACM Transactions on mathematical software (TOMS)* 23.4 (1997), pp. 550–560.

[46] Stephen M Stigler. "Gauss and the invention of least squares". *the Annals of Statistics* (1981), pp. 465–474.

[47] John A Nelder and Roger Mead. "A simplex method for function minimization". *The computer journal* 7.4 (1965), pp. 308–313.

[48] Joseph Perl, Jungwook Shin, Jan Schümann, Bruce Faddegon, and Harald Paganetti. "TOPAS: an innovative proton Monte Carlo platform for research and clinical applications". *Medical physics* 39.11 (2012), pp. 6818–6837.